Simulation of sub-ice shelf melt rates in a general circulation model: velocity-dependent transfer and the role of friction

Véronique Dansereau,[1] Patrick Heimbach,[1] Martin Losch,[2]

Corresponding author: Veronique Dansereau, Department of Earth, Atmospheric and Planetary Sciences, Massachusetts Institute of Technology, office 54-1421, Cambridge, MA 02139, USA. (vero_d@mit.edu)

[1]Department of Earth, Atmospheric and Planetary Sciences, Massachusetts Institute of Technology, Cambridge, MA 02139, USA.

[2]Alfred Wegener Institute, Bremerhaven D-27570, Germany.

Abstract.

Two parameterizations of turbulent boundary layer processes at the interface between an ice shelf and the cavity circulation beneath are investigated in terms of their impact on simulated melt rates and feedbacks. The parameterizations differ in the transfer coefficients for heat and freshwater fluxes. In their simplest form, they are assumed constant and hence are independent of the velocity of ocean currents at the ice shelf base. An augmented melt rate parameterization accounts for frictional turbulence via transfer coefficients that do depend on boundary layer current velocities via a drag law. In simulations with both parameterizations for idealized as well as realistic cavity geometries under Pine Island Ice Shelf, West Antarctica, significant differences in melt rate patterns between the velocity-independent and dependent formulations are found. Whereas patterns are strongly correlated to those of thermal forcing for velocity-independent transfer coefficients, melting in the case of velocity-dependent coefficients is collocated with regions of high boundary layer currents, in particular where rapid plume outflow occurs. Both positive and negative feedbacks between melt rates, boundary layer temperature, velocities and buoyancy fluxes are identified. Melt rates are found to increase with increasing drag coefficient C_d, in agreement with plume model simulations, but optimal values of C_d inferred from plume models are not easily transferable. Uncertainties therefore remain, both regarding simulated melt rate spatial distributions and magnitudes.

1. Introduction

Interactions between the ocean circulation and the ice/ocean interface under floating ice shelves have received considerable attention in the context of observed changes in flow speed and thinning of marine ice sheets around Antarctica (e.g., *Joughin and Alley* [2011] for a review of the fast-growing literature on this subject). Among the most recent studies, *Pritchard et al.* [2012] deduced maximum overall thinning rates of up to 6.8 m/y between 2003 and 2008 for ice shelves along the Amundsen and Bellingshausen Sea coasts, despite thickening of the firn layer and increased influx from glacier tributaries. They concluded that regional thinning is caused by increased basal melt, driven by ice shelf-ocean interactions. Observations by *Jacobs et al.* [2011] indicated a 6% increase between 1999 and 2004 in the temperature difference between the base of Pine Island Ice Shelf (PIIS) in the Amundsen Sea Embayment and the ocean just below, consistent with an increased volume of warmer Circumpolar Deep Water (CDW) outside the cavity. Although significant, the authors pointed out that this warming is too small to explain the 77% increase in the strength of the circulation under PIIS and the 50% increase in meltwater production observed over the same period. Their results suggest that the internal cavity dynamics is at least as, if not more important, than hydrographic conditions of the far field ocean in controlling the ice shelf mass balance.

Deploying instruments at the base of hundreds of meters thick ice shelves is a serious technological challenge, hampering direct measurements of ice shelf-ocean interactions and associated melt rates. The investigation of ice shelf cavities dynamics therefore rely largely on model simulations. In particular, the turbulent mixing that occurs within a thin boundary layer at the ice shelf base was identified as the critical process by which the sensible heat and kinetic energy of the ocean impact the melting and refreezing that control both the mass balance of the ice shelf and the buoyancy forcing on the cavity circulation [*Holland and Jenkins*, 1999; *Jenkins et al.*, 2010a]. Current modeling approaches do not resolve the turbulent boundary processes. Hence turbulence closure schemes, i.e. parameterizations of these fluxes, are required to infer melt rates. Since turbulent processes have not yet been directly measured at the ice shelf-ocean interface [*Jenkins et al.*, 2010a], these parameterizations remain highly uncertain.

The turbulence closure employed in most models is based on a standard approach in which fluxes are related to spatial gradients of temperature and salinity via bulk turbulent exchange velocities (or piston velocities) γ. The simplest (and earliest) parameterization with constant heat and freshwater exchange velocities γ_T and γ_S [*Hellmer and Olbers*, 1989] implicitly assumes a temporally and spatially uniform ocean velocity at the ice shelf base. In this case, the only direct forcing on melt rates is the gradient in temperature between the ice interface at the local freezing point and the ocean just below. Example models that have adopted this approach are BRIOS and BRIOS-2 [*Beckmann et al.*, 1999; *Timmermann et al.*, 2002a, b], ROMS [*Dinniman et al.*, 2007] and HIM [*Little et al.*, 2008].

Ocean currents are the dominant physical driver of turbulent heat and salt transfers at the ice shelf base. Where tidal currents are large, they are thought to be a major source of turbulent kinetic energy in ice shelf cavities [*MacAyeal*, 1984a, b, 1985a, b; *Holland*, 2008; *Jenkins et al.*, 2010a; *Mueller et al.*, 2012; *Makinson et al.*, 2012]. In the velocity-independent melt rate parameterizations, the impact of currents or tides on the distribution of sub-ice shelf melting is indirect, hence limited. A more physically motivated parameterization of the turbulent heat and salt exchanges therefore accounts for the kinematic stress at the ice-ocean interface and defines transfer coefficients γ_T and γ_S in terms of a friction velocity that is directly related to current velocity [*Jenkins*, 1991; *Holland and Jenkins*, 1999; *Jenkins et al.*, 2010a]. Such a parameterization is inspired by formulations employed in models of sea ice-ocean interactions [*McPhee et al.*, 1987; *McPhee*, 1992; *McPhee et al.*, 1999, 2008].

Many models employed today to simulate sub-ice shelf melt rates have adopted velocity-dependent parameterizations of turbulent heat and freshwater transfer, e.g., *Holland and Jenkins* [2001]; *Jenkins and Holland* [2002]; *Holland et al.* [2003, 2008]; *Makinson et al.* [2011] (MICOM), *Smedsrud et al.* [2006]; *Holland et al.* [2010] (MICOM/POLAIR), *Holland and Feltham* [2006] (plume model), *Little et al.* [2009] (HIM), *Timmermann et al.* [2012] (FESOM), and *Dinniman et al.* [2011]; *Mueller et al.* [2012]; *Galton-Fenzi et al.* [2012] (ROMS). Nevertheless, velocity-independent formulations are also still in use. Examples of the latter that either appeared since the review on the subject by *Jenkins et al.* [2010a] or were not mentioned in that review are *Dinniman et al.* [2007] (using ROMS, but later updated to velocity-independent, *Dinniman et al.* [2011]), *Heimbach and Losch* [2012] and *Schodlok et al.* [2012] (using MITgcm) and *Kusahara and Hasumi* [2013] (using COCO). More importantly, in most cases where models have been updated from velocity-independent to dependent formulations, the impact has not been documented. To our knowledge, the work of *Mueller et al.* [2012] on Larsen C ice shelf is the only published direct model comparison of the spatial distribution of melt rates and cavity circulation simulated with and without a velocity-dependent melt rate parameterization. The results of our study indicate that further comparisons and sensitivity analyses of the two types of parameterizations are warranted to better understand the heat and freshwater transfers simulated in models currently in use.

Performing such comparisons for models with different vertical discretization is a further motivation of our study. The ROMS model used by *Mueller et al.* [2012] is based on terrain-following (or "σ") vertical coordinates, which may exhibit different behavior to that of isopycnal models (e.g., MICOM, HIM), or z-level or height) models. In this study, we use a z-level model, the Massachusetts Institute of Technology general circulation model [MITgcm, *Marshall et al.*, 1997a; *Adcroft et al.*, 2004].

Another important distinction in the context of ice shelf-ocean interactions is that between "cold" and "warm" ice shelves. Larsen C is an example of the former, floating in waters near the surface freezing point. One interest behind the present study is in refining our understanding of simulated melt rates under PIIS. This ice shelf is in contact with CDW nearly 3°C above the surface freezing point and hence is an example of the later. It is therefore unclear to which extent results obtained by *Mueller et al.* [2012] for Larsen C are readily transferrable to PIIS and adjacent warm ice shelves.

PIIS is home to the strongest ocean thermal forcing and mass loss in Antarctica [*Rignot and Jacobs*, 2002; *Joughin et al.*, 2010; *Jacobs et al.*, 2011]. Two recent studies [*Heimbach and Losch*, 2012; *Schodlok et al.*, 2012] have simulated sub-ice shelf melt rate magnitudes and spatial patterns using the MITgcm, although neither of these have used velocity-dependent transfer coefficients. An in-depth understanding of the dependence of melt rates on the parameterization employed is a crucial step to increase our confidence in simulated melt rates in this important region.

Finally, the anticipated increased use of the MITgcm, an open-source code, for ice shelf-ocean interaction studies merits a detailed assessment of issues surrounding the formulation of turbulent exchange velocities in melt rate parameterizations.

The purpose of this study is to provide such an assessment. Main goals here are to identify differences in melt rate patterns associated with the use of velocity-dependent versus velocity-independent parameterizations, and to understand the physical processes responsible for these differences and possible cavity circulation changes. Another goal is to identify potential feedback mechanisms between melting, circulation, meltwater plume velocity and hydrographic properties and transfer coefficients.

The paper is structured as follow: The MITgcm and its ice shelf cavity component are briefly reviewed in Section 2, along with a description of the model configurations used in this study. Comparisons of simulations using the velocity-independent and velocity-dependent parameterizations, and drag coefficient sensitivity experiments are presented in Section 3. Simulations are conducted using both an idealized ice shelf cavity and a realistic configuration of the cavity underneath PIIS. A discussion of the results is provided in Section 4, and conclusions are summarized in Section 5.

2. The MITgcm model and experimental setup

The MITgcm forms the basis for our study. It is the first z-coordinate ocean model capable of simulating sub-ice shelf cavity circulation and under-ice shelf melting [*Losch*, 2008]. At resolutions above 1 km the three-dimensional flow is hydrostatic [*Marshall et al.*, 1997b]. As in virtually all sub-ice shelf cavity circulation simulations published so far, the ice shelf base is maintained fixed regardless of the melting and refreezing. Convective adjustment parameterizes vertical motion in case of unstable stratification.

2.1. Sub-ice shelf melt rate parameterization in the MITgcm

The initial velocity-independent formulation implemented in the MITgcm assigns constant values to $\gamma_{T,S}$. Details are described in Appendix A. We note that a previous description (but not the actual implementation in the code) in *Losch* [2008] contains errors that have been corrected in Appendix A.

In the velocity-dependent formulation the piston velocities $\gamma_{T,S}$ are functions of the frictional drag at the ice shelf base via a friction velocity, u_*, which is related to the velocity of ocean currents through a simple quadratic drag law involving a drag coefficient C_d. A brief outline is given in Appendix B. This implementation mostly follows the approach suggested by *Holland and Jenkins* [1999]. In the light of their sensitivity analyses of melt rates to the details of the parameterization, several approximations have been adopted here and are summarized in Appendix C.

The heat and salt balances and associated sign conventions used in the present model are illustrated in Figure 1. In particular, the melt rate m, as defined in terms of freshwater mass flux in eqns. (A1)–(A2), is negative for melting and positive for refreezing. Variables and constants of the melt rate parameterizations are listed in Table 1.

Two important aspects, the treatment of the ice-ocean mixed-layer and the choice of drag coefficients are discussed in more detail in the following.

Treatment of "mixed layer" properties: Although we will adopt the term "mixed layer" used by *Holland and Jenkins* [1999], we acknowledge that in our z-coordinate model the definition of a mixed layer is ambiguous. We often refer to the first ocean grid cell underneath the ice shelf as the "mixed layer", because hydrography and momentum are homogenized in this layer (see below). With the no-slip condition at the ice shelf base, ocean currents are weaker in the grid cells directly in contact with the ice interface than in the cells further away from the shelf base. Where melt rates are large enough along the path of outflow plumes, the grid cells adjacent to the interface are also filled with buoyant, cold and fresh meltwater. Hence increasing the depth of the model mixed layer, which can be achieved by increasing the number of vertical grid cells over which hydrographic properties and ocean currents are averaged to obtain T_M, S_M, and U_M, is expected to locally increase both the thermal and dynamical forcing and hence the melt rates. Sensitivity experiments in this regard will be presented in Section 3.2.

Choice of drag coefficient: The choice of drag coefficient C_d also deserves special attention. Although roughness characteristics underneath ice shelves are likely spatially variable [*Nicholls et al.*, 2006], a constant C_d is usually employed. *MacAyeal* [1984a, b] first used values suggested by *Ramming and Kowalik* [1980] for open water ($C_d = 2.5 \cdot 10^{-3}$) and ice shelf covered water ($C_d = 5.0 \cdot 10^{-3}$) in a barotropic model of the circulation beneath Ross Ice Shelf, hence attributing the same drag to the seabed and ice shelf base. *Holland and Jenkins* [1999] and *Holland and Feltham* [2006] later adopted a lower value of C_d of $1.5 \cdot 10^{-3}$ at the ice shelf base to account for smoothing effects by melting and ice pumping. More recently, *Jenkins et al.* [2010a] tuned C_d in their model, and found the best agreement between melt rates simulated using the velocity-dependent parameterization and measurements of ablation rates underneath Ronne ice shelf for $C_d = 6.2 \cdot 10^{-3}$. A conclusion is the recognition that C_d is a highly uncertain parameter. While it might require adjustments, a simple tuning of the drag coefficient might compensate for other deficiencies of the current models [*Jenkins et al.*, 2010a]. This issue will be taken up in more detail in Section 3.2.

2.2. Model configurations

All model configurations used here have a horizontal resolution of $1/32°$ corresponding to grid cells of roughly 1×1 km^2 size, and a uniform vertical discretization of 50 vertical levels of 20 meters thickness. Partial cells [*Adcroft et al.*, 1997] are used to accurately represent both sea floor topography and ice shelf geometry. A volume-weighted vertical interpolation between neighboring boundary layer grid points reduces numerical noise that is associated with the partial-cell treatment. Biharmonic viscosity is used to dampen the noise in the velocity fields associated with excitation of grid-scale waves. Very weak and stationary noise patterns remain in the model results, but do not affect the numerical stability of the solution. Details on the sources of noise are discussed by *Losch* [2008].

2.2.1. Realistic simulation configuration

The model domain encompassing PIIS is delimited by the $102°20'$ W and $99°22'$ W meridians and the $74°30'$ S and $75°27'$ S parallels. The portion of the cavity south of about $74°48'$ S is referred to in the following as "PIIS proper" and is more extensively analyzed than the more stagnant area to the north [*Payne et al.*, 2007]. The ice shelf geometry and the sea floor bathymetry are based on the *Timmermann et al.* [2010] data set, which includes the information about draft and cavity bathymetry from in-situ Autosub data [*Jenkins et al.*, 2010b]. The sea floor reaches a maximum depth of about 1000 m and the ice shelf draft varies between 200 m at the ice shelf front and about 900 m at the grounding line. Another important feature of this data set is the presence of a sill of about 300 m rising above its surroundings, oriented in the southwest-northeast direction approximately half-way between the ice shelf front and the deepest reaches of the grounding line in the southeastern corner of PIIS proper (Figure 2a). The domain has one open boundary to the west; all other boundaries are closed. Time-mean vertical profiles of zonal velocity, potential temperature and salinity are prescribed at the western open boundary (solid curves in Figures 3a and 3b respectively). These are the same profiles used by *Heimbach and Losch* [2012]. They were estimated from in situ data provided by five hydrographic stations located along the ice shelf front and are uniform in the meridional direction. Relatively fresh and cold water leaves the cavity at the surface and warm, salty water enters the cavity at depth.

2.2.2. Idealized simulation configuration

The idealized configuration serves to examine in more detail the impact of velocity-dependence in the turbulent ice-ocean transfer on the melt rates and ocean circulation underneath the ice shelf. The rectangular domain is delimited by the 105°30′ W and 99°22′ W meridians and by the 74°30′ S and 75°27′ S parallels. Its eastern half is covered by a meridionally-uniform ice shelf and the western half is an open ocean that exchanges neither heat nor mass with the atmosphere. The westernmost 20 grid cells act as a sponge layer with a relaxation time of 10 days. The cavity geometry is representative of a typical ice shelf, and scaled to be consistent with the specific case of PIIS. The ice shelf base depth increases monotonically from 200 m at the ice shelf front to 900 m depth at the grounding line. The sea floor is flat and at a depth of 1000 m (see Figure 2b).

As for the realistic configuration, time-mean, meridionally uniform profiles of zonal velocity, ocean temperature and salinity are prescribed at the western open boundary (dashed curves in Figures 3a and 3b). These profiles were chosen to be consistent in magnitude and shape with the mean profiles used in the realistic experiments, hence to represent the conditions at the mouth of a typical "warm" ice shelf in contact with

CDW. The sinusoidal profile of zonal velocity ensures a zero net volume flux at the open boundary. The circulation and melt rates are not sensitive to the specific amplitude of this prescribed zonal current profile, as long as it does not significantly exceed the magnitude of the barotropic circulation in the cavity.

All simulations are started from rest. The initial hydrographic profiles are meridionally and zonally uniform, and correspond to the western open boundary profiles. A spinup of three years is performed to reach steady-state hydrographic conditions and melt rates. Monthly averaged fields for the last month of the spinups are analyzed. Unless otherwise stated, a default drag coefficient of $C_d^0 = 1.5 \cdot 10^{-3}$ is employed, as in *Holland and Jenkins* [1999] and *Holland and Feltham* [2006]. As mentioned in section 2.1, this value lies in the low range of values employed in previous modeling studies. In all simulations, the drag coefficient in the melt rate parameterization is the same as for the frictional drag at the ice-ocean interface in the momentum equations. Table 2 summarizes the characteristics of each set of experiments.

3. Results

The experiments conducted fall into two main categories: velocity-dependent versus independent parameterizations (Section 3.1), and sensitivity to the choice of drag coefficient (Section 3.2). For a clear understanding of the results, all simulations were conducted for both the idealized and realistic configurations.

3.1. Velocity-independent versus dependent parameterizations

3.1.1. Idealized experiments

Various authors have investigated the ocean circulation and melt rate distribution underneath idealized ice shelves. Their cavity geometries were typically north-south oriented with base depths decreasing monotonically southward from a few hundred meter thick ice shelf front to a 1 to 2 km deep grounding line. Among these are *Hellmer and Olbers* [1989]; *Determann and Gerdes* [1994]; *Grosfeld et al.* [1997]; *Holland and Jenkins* [2001]; *Timmermann et al.* [2002b]; *Holland et al.* [2008]; *Losch* [2008]; *Little et al.* [2008]. Recurring results of these idealized studies were: (1) the set up of a density-driven overturning circulation due to the depression of the freezing point temperature of seawater with pressure and resulting temperature differences between the ice interface and ambient ocean at depth; (2) predominantly geostrophic mixed layer currents constrained by the distribution of background potential vorticity, i.e., by the water column thickness gradient; (3) maximum melt rates occurring along the south eastern boundary of the cavity, where warm waters first reach the ice shelf base at the grounding line; and (4) maximum refreezing rates concentrated at the western boundary, along the path of the buoyant meltwater plume that rises along the ice shelf base. Rotation and cavity geometry, in turn, were identified to exert strong constraints on the spatial distribution of melting and refreezing, in agreement with potential vorticity considerations.

Our simulation of sub-ice shelf cavity melt rates and circulation (Figure 4a) using the velocity-independent parameterization is consistent with this picture (but note the difference in cavity orientation, which in the present study is west–east to align with the realistic Pine Island cavity geometry). Maximum melt rates are found near the grounding line over the northeastern corner of the cavity where the warmest waters reach the ice shelf base (see Figures 5a and 5b for the thermal forcing, $T_M - T_B$). The horizontal streamfunction for the vertically-integrated volume transport (contours in Figure 4a) indicates a cyclonic gyre covering the whole domain. In the eastward branch of the gyre, warm water from the open ocean entering the cavity is diverted along the northern boundary, consistent with a buoyancy-induced cyclonic circulation set up by melting at the ice shelf base. From the northeastern corner of the cavity, where maximum melt rates occur, the water mass formed through mixing of meltwater and ambient water flows southward along the ice shelf base. Melt rates decrease southward as the plume becomes more diluted with meltwater and exhausts its heat potential. The barotropic streamfunction indicates an intensification of the westward flowing branch along the southern boundary, in agreement with the intensification of an ageostrophic flow against the topographically-induced background potential vorticity gradient.

The fact that the circulation and melt rate patterns are consistent with results of *Little et al.* [2008] and ISOMIP experiments, which in comparison are representative of large, "cold" ice shelves, suggests that the buoyancy and dynamical constrains discussed above are applicable to a broad range of ice-ocean systems.

The main differences between our velocity-independent simulations and that of previous studies is that ice does not accumulate at the ice shelf base and that densified water does not downwell at the ice shelf front. Instead, the plume escapes the cavity and interacts with the open ocean. As pointed out by *Holland et al.* [2008], such conditions are consistent with small, steep ice shelves in contact with CDW with temperatures exceeding 1°C. Observational support for this behavior can be found in *Jacobs et al.* [1996]. Consistent with the absence of freezing-induced downwelling at the ice shelf edge and with the meltwater plume "overshooting" out of the cavity, the cyclonic gyre characterizing the vertically integrated volume transport is not restricted to the cavity but extends into the open ocean. This suggests greater barotropic exchanges between the open ocean and the ice shelf cavity relative to the typical "cold" ice shelf circulation [*Grosfeld et al.*, 1997; *Losch*, 2008].

The idealized model run with the velocity-dependent parameterization and the default drag coefficient C_d^0 produces a depth-integrated volume transport (contours in Figure 4b) and a meridionally averaged overturning circulation (not shown) that are very similar to those of the run with the velocity-independent parameterization. However, the spatial distribution of melt rates differs substantially between the two simulations. In the velocity-dependent case, the maximum melt rates are found along the exit path of the meltwater plume, that is, over the intensified westward branch of the cyclonic circulation along the southern edge of the cavity, and over an area extending westward from the southern part of the grounding line. There is no melt rate maximum associated with the northeastern inflowing branch of the cavity circulation.

The correspondence between the overturning and horizontal circulations simulated in the two experiments implies that hydrographic properties inside the cavity are similarly distributed in both cases. The discrepancies in melting patterns therefore suggest that the melt rate is not as sensitive to ocean temperature in the velocity-dependent than in the velocity-independent simulations. Instead, the frictional effect of the mixed layer currents might dominate over the thermal forcing in setting the heat flux through the ice-ocean boundary layer in the velocity-dependent case.

To test this hypothesis, we compare the velocity-independent and dependent melt rate patterns to the patterns of the two main drivers of the diffusive heat flux (Q_T^M). These are (see equations A4 and B2 in the appendix) the difference in temperature across the boundary layer, $T_M - T_B$ (Figures 5a,b), and, through the formulation of the friction velocity, the magnitude of mixed layer current velocity, U_M (Figures 5c,d). As expected, the spatial patterns of both the thermal forcing and mixed layer velocity are very similar in the velocity-independent and dependent simulations. In both cases, the highest temperature gradients across the ice-ocean boundary layer are found over the northeastern corner of the cavity, at depth, where the warmest mixed layer waters are found. The mixed layer water cools as it flows southward. The fastest mixed layer currents are concentrated along the southern cavity wall over the region of plume outflow, and increase southward over the interior part of the cavity.

The spatial correlation between the melt rates and either forcing is however very different between the two simulations: in the velocity-independent case, melt rate maxima are collocated with maxima in thermal forcing and are insensitive to the details of the mixed layer velocity pattern. In the velocity-dependent case, melt rates are not collocated with thermal forcing, but instead are well aligned with the distribution of U_M, such that the highest rates are found over the regions of fastest mixed layer currents, i.e., over the path of the outflow plume.

This shift of maximum melt rates from areas of high ocean heat to regions of strong currents is consistent with results by *Mueller et al.* [2012]. They found that between two experiments in which they used the velocity-dependent parameterization of *Holland and Jenkins* [1999] (modified by adopting the scalar transfer coefficients of *McPhee et al.* [2008]) and the velocity-independent parameterization of *Hellmer and Olbers* [1989], maximum melt rates shifted from the vicinity of the deep grounding line, where T_B is low, i.e, the thermal forcing is high, to regions of strongest time-mean barotropic currents.

A similar behavior was simulated by *Gladish et al.* [2012] who applied the model of *Holland and Feltham* [2006] to the floating tongue of Petermann Gletscher (Northwest Greenland). They found a somewhat larger spatial correlation between melt rate and mixed layer current forcing than between melt rate and thermal forcing. However, in their model vertical profiles of T and S were prescribed and homogeneous in the horizontal and their thermal forcing was high and approximately uniform in the regions of high melt rates, which is not necessarily the case in the present experiments.

Moving from melt rate patterns to magnitudes reveals that melting is overall lower in the velocity-dependent simulation with ${C_d}^0$ than in the velocity-independent one. The lower melting explains the difference in the strength of the mixed layer currents and thermal forcing between the two experiments. In the velocity-independent simulation, higher melt rates lead to stronger buoyancy-flux induced density gradients and support faster mixed layer currents over the interior part of the cavity. The production of larger volumes of buoyant melt water overall cools the mixed layer and hence reduces thermal forcing relative to the low melt rates in the velocity-dependent simulation. Section 3.2 discusses these effects in detail in the context of the sensitivity of velocity-dependent melt rates to the drag coefficient.

3.1.2. Experiments with realistic geometry

Melt rates simulated with the realistic PIIS configuration using the velocity-independent and velocity-dependent parameterizations (with the default ${C_d}^0$) are shown in Figures 6a and 6b, respectively. Corresponding patterns of temperature difference across the boundary layer, $T_M - T_B$, and of mixed layer velocities, U_M, are illustrated in Figures 7a–d.

As in the idealized experiments, spatial patterns of $T_M - T_B$ and of U_M are very similar between the two parameterizations, but important differences are seen in the melt rate distributions. Velocity-independent melt rates are highly spatially correlated with the thermal forcing. Figure 6a shows melting to be largest over the southeastern portion of the cavity where the ice shelf base is deepest, i.e. where T_B is lowest. Vertical cross sections of temperature and salinity (not shown) confirm that the warmest and most salty waters reach the grounding line in this area.

Figure 6c shows the vertically-integrated volume transport along with the water column thickness (black, dashed contours). As in the idealized experiments, the structure of the circulation suggests that the barotropic transport inside the cavity is strongly controlled by the distribution of water column thickness (nearly equivalent to the distribution of background potential vorticity, f/h). Three prominent gyres are labeled in the Figure: (1) a strong cyclonic gyre over the exit of the cavity; (2) a second prominent cyclonic gyre deep inside the cavity, inward of the sill; and (3) a weaker anti-cyclonic gyre also inward of the sill and to the north of cyclonic gyre 2. Transport over the sill is weak, with cross-sill exchanges confined to its northern and southern sides.

Figures 7b and 7d indicate that the melt rate pattern simulated with the velocity-dependent parameterization is not correlated with the thermal forcing. Instead, it mimics the distribution of the mixed layer currents. In agreement with the idealized cavity configuration, melt rate maxima are collocated with rapid plume outflows. The strongest outflow occurs at the southern flank of cyclonic gyre (1) around 75°06′S, 101°30′W. This position marks a convergence zone with waters originating from the southern flank of cyclonic gyre (2). The water leaves the cavity at the southern edge of the ice front. The outflow at the northern flank of anti-cyclonic recirculation gyre (3) around 74°55′S, 100°30′W, coincides with the convergence of currents against the eastern cavity wall of PIIS proper. A third weaker outflow collects melt water from the more stagnant northern portion of the cavity. Only part of these two outflows leaves the cavity when reaching the ice shelf front. The other part is steered southward along the ice front and the first stronger outflow near the southern boundary. Two patches of relatively higher melt rates are also seen downstream of the deepest portions of the grounding line, corresponding to locally intensified mixed layer currents.

As in the idealized experiment, the realistic velocity-dependent simulation with C_d^0 produces smaller melt rates than the corresponding velocity-independent simulation. The maximum velocity-dependent integrated volume transport is reduced by about 40% relative to the velocity-independent transport. The overall structure of the transport is similar in both cases.

3.1.3. Observational evidence

Observational melt rate estimates under PIIS are limited. In the following, we compare our simulated melt rate pattern with recent studies that produced estimates of melt rate distribution under PIIS from available observations and to the plume model simulations of *Payne et al.* [2007], which to our knowledge produced the only published high-resolution velocity-dependent melt rate distribution for the entire ice shelf.

A notable similarity between our realistic velocity-dependent simulations and that of *Payne et al.* [2007] is that local melt rate maxima are collocated with the paths of two principal outflow plumes underneath PIIS and with a third weaker outflow collecting meltwater under the northern portion of the ice shelf (see Figures 4 and 6 from [*Payne et al.*, 2007]). Our results also agree with their melt rate estimates from ice flux divergence calculations based on ice velocity and shelf thickness data. These calculations indicated local melt rate maxima near the southernmost part of the ice shelf front and along the northern cavity wall of PIIS proper (see their Figure 10).

Payne et al. [2007] pointed out that Advanced Spaceborne Thermal Emission and Reflection Radiometer (ASTER) images indicate a retreat of sea ice in front of the ice shelf over three isolated areas collocated with their plume outflows, suggesting the presence of warm upwelling plume water there. *Bindschadler et al.* [2011] analyzed 116 Landsat images spanning 35 years and a few images from Advanced Very High Resolution Radiometer (AVHRR) and Moderate Resolution Imaging Spectroradiometer (MODIS) and observed three recurrent polynyas at the same fixed locations. The largest of these polynyas was positioned at the southern edge of the ice shelf front, where our realistic model and that of *Payne et al.* [2007] simulate the strongest outflow and where *Jacobs et al.* [2011] also observed concentrated meltwater outflows. Analyses of temperature, salinity and current profiles from a research cruise in 2009 and of Landsat thermal band and thermal infrared (TIR) images from two austral summers during which the ocean was sea ice-free at the ice shelf front support the presence of warmer waters exiting the ice shelf cavity in the same locations of the three polynyas present during other summers [*Bindschadler et al.*, 2011; *Mankoff et al.*, 2012].

A notable difference to the results of *Payne et al.* [2007] is the structure of the mixed-layer flow. In their simulations it is concentrated mostly in the primary outflow along the southern boundary and to a lesser degree along the outflow crossing the middle part of PIIS proper. In our experiments, this latter outflow is stronger and concentrated along the northern boundary of PIIS. This discrepancy can be explained by the different nature of the two models and their interaction with cavity geometry. The mixed layer flow in ice shelf cavities is expected to be predominantly geostrophic and constrained by the background potential vorticity, i.e. by the water column thickness gradient which is set by the bed geometry and by the ice shelf base topography [*Little et al.*, 2008]. As the effect of bathymetry is not accounted for in vertically integrated (plume) models such as that of *Payne et al.* [2007], the mixed layer flow (i.e., the buoyant plume) is steered only by the ice shelf base topography. Important features of the sub-ice shelf topography in the *Payne et al.* [2007] simulations are two inverted channels collocated with their southerly outflow and with the one roughly in the center of the ice shelf (see their Figure 4).

Recent observations [*Dutrieux et al.*, 2013] support the presence of two 3 km-wide channels merging at the southernmost edge of the ice front of PIIS. Landsat images indicate a significant longitudinal surface trough running in the middle of the ice shelf, which, in hydrostatic equilibrium, suggests the presence of a deep inverted trough in the underside of the ice shelf susceptible of channeling buoyant outflow waters [*Bindschadler et al.*, 2011]. These channels are not represented in our shelf base topography (contours in Figures 6a,b). Instead, the cavity geometry feature that appears to exert a strong constraint on the circulation and to give rise to the gyres described above, is the pronounced ridge in our bathymetry data [see also *Schodlok et al.*, 2012]. Our two strongest outflows correspond to areas of convergence along the cavity walls of mostly geostrophic currents.

We also notice a difference in the location of the (near) grounding line maximum melt rates between our simulations and both the simulations and flux divergence estimates of *Payne et al.* [2007], which we attribute to the use of very different PIIS cavity geometries between the two studies. Comparing the present shelf base topography (contours in Figures 6a,b) to the one derived by *Payne et al.* [2007] (see their Figure 2), we note that the deepest portion of the grounding line is not at the same location in the two models. In our setup, the shelf base is deepest (900 meters) in the southeastern corner of PIIS proper (around 75° 18' S, 99° 30' W). In *Payne et al.* [2007] it is also about 900 meters deep at that location, but is even deeper ($>$ 1000 meters) in a hollow portion of the cavity to the northeast (around 75°06' S, 99° 45' W) where the shelf base is only 600 to 400 meters deep in our model. The presence of an inverted channel downstream of this deep portion of the grounding line in the shelf topography of *Payne et al.* [2007] results in a steep gradient of shelf base depth that is not seen in the present ice cavity geometry derived from recent Autosub data [*Jenkins et al.*, 2010b]. This has implications for ice flux divergence calculations.

Moreover, we note that melt rate magnitudes in our velocity-dependent simulation with ${C_d}^0$ are overall lower than previously published estimates [*Payne et al.*, 2007; *Jacobs et al.*, 2011; *Dutrieux et al.*, 2013]. In order to match previous and their own observational estimates of the cavity-average melt rate under PIIS, *Payne et al.* [2007] tuned four poorly constrained parameters of their plume model. For example, they varied the drag coefficient between 1 and $6 \cdot 10^{-3}$. In the following, we investigate how our simulated velocity-dependent melt rates are affected when varying this parameter.

3.2. Melt rate dependence on the drag coefficient

Energy conservation at the ice-ocean interface, eqn. (A1), requires that the latent heat flux associated with melting and refreezing be equal to the diffusive heat flux through the boundary layer, Q_M^T, minus the fraction of heat lost to the ice shelf by conduction, Q_I^T. Usually, the conductive heat flux term is one order of magnitude smaller than the diffusive heat flux term [e.g., *Holland and Feltham*, 2006; *Holland and Jenkins*, 1999; *Determann and Gerdes*, 1994], so that we can express the melt rate as

$$m = -\frac{c_{pM}}{L_f} u_* \Gamma_T (T_M - T_B). \tag{1}$$

Because of the dominance of molecular over turbulent diffusion in the viscous sublayer closest to the ice interface, the heat and salt exchange coefficients $\Gamma_{T,S}$ are only weakly dependent on the friction velocity. Eqn. (1) then predicts to first order a linear dependence of the melt rate on u_* or $\sqrt{C_d}$.

To investigate the dependence of the melt rates on C_d and assess the relative importance of various feedbacks associated with variations of the drag coefficient, we conducted both idealized and realistic PIIS simulations in which C_d was varied between 1/16 and 16 times the default value of $C_d^0 = 1.5 \cdot 10^{-3}$.

3.2.1. Idealized experiments

Figure 8a shows the area-averaged melt rate m (black dots) calculated for velocity-dependent simulations as a function of $\sqrt{C_d/{C_d}^0}$. The area-averaged melt rate of the velocity-independent simulation with ${C_d}^0$ is also plotted as a reference (dashed black line). As predicted by theory, m in the velocity-dependent simulations increases with $\sqrt{C_d}$. In order to understand this behavior, we examine the effect of the two direct forcings on the melt rates as C_d is changed by comparing area-averaged values of the friction velocity and of the difference in temperature across the ice shelf boundary layer.

Positive feedback – friction velocity: Similar to melt rates, friction velocity increases with $\sqrt{C_d}$ (Figure 8c). Fitting the area-averaged friction velocity against $\sqrt{C_d}$ with a power law fit of the form $u_* = a\, C_d^{b/2}$ indicates that the dependence of u_* is above-linear (within a 95% confidence interval, $b = [1.163, 1.373]$). This is because the area-averaged mixed layer velocity in our simulations (Figure 8c, orange dots) also increases with $\sqrt{C_d}$, in a sub-linear manner.

On the one hand, the increase of mixed layer currents with C_d is consistent with the strengthening of buoyancy-flux induced density gradients under the shelf that occurs with the intensification of the melting. In turn, stronger mixed layer currents enhance the diffusive heat flux across the boundary layer, thereby amplifying the increase of melt rates with C_d. This positive feedback between melt rates, buoyancy flux-induced gradients and mixed layer currents is not accounted for in a velocity-independent parameterization. On the other hand, the fact that the increase of U_M with $\sqrt{C_d}$ is sub-linear is consistent with the enhanced frictional drag.

Negative feedback – thermal forcing: Figure 8e shows a decrease of the cavity-averaged thermal forcing (purple dots) with increasing drag coefficient. This points to an overall cooling of the mixed layer. It is consistent with the production of a larger volume of cold buoyant meltwater that spreads at the ice shelf base, stratifying the upper water column and forming an insulating film [*Gill*, 1973; *Little et al.*, 2009]. This reduction in thermal forcing is a negative feedback on the increase of melting with C_d.

Provided that the cooling is due to a larger production of meltwater, the salinity at the ice shelf base, S_B, will also decrease with increasing C_d. Through the dependence of the freezing point, T_{freeze}, on salinity (eqn. A3), this should raise T_{freeze} and reduce the difference of temperature across the boundary layer, thereby slowing the increase in melt rates with C_d. Because the dependence of the freezing point of seawater on salinity is only weak, this effect is expected to be small.

To verify whether this salt feedback actually has a non-negligible effect on the *thermal forcing*, $T_M - T_B$, with changing C_d, we calculate the area-averaged *thermal driving* underneath the ice shelf (red dots),

$$T_* = T_M - T_B - a\,(S_M - S_B) \tag{2}$$

with $(S_M - S_B)$, the salinity difference across the boundary layer and a, the (negative) salinity coefficient given in Appendix A. Thermal driving is the thermal forcing obtained when neglecting the effects of salt diffusivity on the temperature gradient at the ice shelf base [*Holland and Jenkins*, 1999]. In the present experiments, its area average is higher than the area averaged thermal forcing by about 0.3 to 0.8°C, indicating that neglecting the effects of salt diffusivity would significantly overestimate the melt rates. Figure 8d shows that the thermal forcing and driving behave very similarly as a function of C_d in the model. This suggests that salinity feedbacks on the simulated melt rates are not significant, as anticipated.

Melt rate versus C_d fit: Returning to Figure 8a, a power law fit of the form $m = a\,C_d^{b/2}$ to the area-averaged melt rate against $\sqrt{C_d}$ gives $b < 1$ with a 95% confidence interval ($b = [0.579, 0.922]$), suggesting that the negative feedback of the decreased thermal forcing on the melt rates exceeds the positive feedback associated with the increased mixed layer velocity. The scattering of the calculated melt rates around the fitted curve in Figure 8a reveals, however, systematic deviations from the simple power law fit over different ranges of $\sqrt{C_d}$. It suggests other feedbacks or non-linearities, or both, to be at play in the model, and that are not accounted for in the above considerations.

Spatial patterns: Over the range of C_d values investigated, the *spatial patterns* described in the previous section for the velocity-dependent $\gamma_{T,S}$ simulation (see Figures 6b and 5b,d) remain overall unchanged. We therefore only report the results, while omitting supporting figures. Substantial melting near the grounding line is a persistent feature, with a decrease westward towards the ice front. Maximum melting is collocated with the outflow of the meltwater plume along the southern boundary. As C_d is increased, both melting and mixed layer currents increase in these regions, as expected from the strengthening of buoyancy-induced zonal density gradients. Melt rates therefore remain highly spatially correlated with the mixed layer velocity. Slow refreezing occurs over a limited region bordering the northern edge of the plume for $C_d > 4 \cdot {C_d}^0$.

The temperature difference across the boundary layer diminishes over the region of largest melt when C_d is increased. For $C_d > 2 \cdot {C_d}^0$, both the temperature and salinity of the mixed layer locally decrease below the lowest surface temperature and salinity prescribed as initial conditions. This confirms that the cooling of the mixed layer is due to an increased production of melt water rather than a redistribution of hydrographic properties in the cavity. Consistent with this picture, zonal sections of temperature and salinity across the westward outflow indicate a cooling, freshening and thickening of the plume as the drag coefficient is increased (not shown). For the case of $C_d = 16 \cdot {C_d}^0$, this negative feedback of thermal forcing on melting seems to have a noticeable impact on the melt rate pattern. In this case, melt rates near the grounding line become comparable to that along the path of the outflow plume and are highest towards the northern half of the cavity, where thermal forcing is maximal.

Both the depth-integrated volume transport and the meridionally-integrated zonal overturning circulation strengthen with increasing C_d, but again with a spatial pattern virtually unchanged compared to that for ${C_d}^0$ (Figure 4d). The increase in the barotropic circulation is consistent with increased melting and enhanced buoyancy-induced density gradients [*Little et al.*, 2008]. The strengthening of the overturning circulation agrees with the production of larger volumes of melt water, the increase of vertical density gradients, and the enhanced buoyancy of the plume [*Holland et al.*, 2008].

3.2.2. Realistic experiments

Thermodynamic forcings, melt rates and circulation in the experiments with realistic ice shelf and sea floor geometries of PIIS behave in a very similar manner as in the idealized experiments when varying C_d, as revealed by comparing the left and right panels of Figure 8. The same holds true for a number of inferences made, including (1) the positive feedback between enhanced melting, strengthened buoyancy-induced density gradients and mixed layer currents, (2) the increased production of meltwater that insulates the ice interface from the warmer waters below, (3) the negligible impact of salinity through the dependence of the freezing point of seawater, (4) the overall conservation of the spatial patterns of melting, thermal and ocean current forcings represented in Figures 6b and 7b, d, and of the structure of the barotropic circulation shown in Figure 6d.

The fact that the spatial distribution of melt rates in the velocity-dependent experiments is robust and does not seem to depend on the specific drag coefficient over a a wide range of values is a valuable result, since in practice, the appropriate value for C_d underneath ice shelves remains unknown.

In both the idealized and realistic experiments, the thermal forcing is higher in the velocity-dependent than in the velocity-independent simulation over the entire range of C_d values investigated. This is a consequence of the regions of rapid melting and of high thermal forcing being spatially decorrelated in the velocity-dependent case. Even if the production of cold meltwater increases with C_d and mixed layer temperatures drops locally over region of strong mixed layer currents and rapid melting, T_M remains comparatively high where thermal forcing is strong.

In the realistic experiments, the area-averaged mixed layer velocity is lower in the velocity-dependent than in the velocity-independent simulation for all values of C_d. This is not the case in the idealized simulations, for which a drag coefficient about four times the default value matches the mixed layer velocities. Moreover, a drag coefficient about 8 times the default value is required to match the velocity-dependent and velocity-independent melt rates in the realistic case. In the idealized experiments, $C_d \approx 2 \cdot {C_d}^0$ is required. These differences indicate that no value of drag coefficient reconciles the two melt rate parameterizations in all simulations and suggests that the ice shelf cavity system reaches different thermodynamic steady states between our idealized and realistic experiments that are not readily comparable. This might be indicative of additional feedbacks between melt rates, mixed layer velocities, buoyancy fluxes and topographic features that occur in the more realistic case.

A drag coefficient about 4 to 8 times our default value would be needed to match our cavity-averaged melt rate under PIIS to the ice flux divergence based estimate of

Payne et al. [2007] of 20.7 m/yr (Figure 8b). Using $C_d = 4 \cdot {C_d}^0$ and $C_d = 8 \cdot {C_d}^0$, the spatial average over PIIS proper varies from 23 m/yr to 31 m/yr. These values compare favorably with the 29.7 m/yr PIIS-proper value of *Payne et al.* [2007], and with the 24 ± 4 m/yr estimate of *Rignot* [1998]. Figure 9a shows the distribution of melt rates for $C_d = 6 \cdot 10^{-3} = 4 \cdot {C_d}^0$. Maximum melt rates of 60 to almost 100 m/yr are found over the path of the outflow plume that exits at the southern end of the ice shelf front and rates of up to 70 m/yr are collocated with the outflow along the northern boundary of PIIS proper. Melting near the southeastern portion of the grounding line exceeds 50 m/yr and decreases rapidly downstream to 10-20 m/yr, outside the regions associated with the outflows, in agreement with the result of ice flux divergence calculations of *Rignot* [1998] and the more recent estimates along four airborne survey lines over PIIS by *Bindschadler et al.* [2011]. In the case of $C_d = 8 \cdot {C_d}^0$, the pattern is virtually the same, and these values become 80 to 113 m/yr and 90 m/yr for the two main outflows, 80 m/yr near the grounding line, and $20 - 30$ m/yr downstream of the grounding line melt region.

Figure 9b shows the difference between melt rates simulated using ${C_d}^0$ and $C_d = 4 \cdot {C_d}^0$. Melting increases more rapidly with C_d over the regions that are already local melt rate maxima for $C_d = {C_d}^0$. The increase is comparable along the outflows and over the regions downstream of the grounding line. Therefore, as melt rates are lower there than along plume paths in the default C_d simulation, this indicates that melting increases more rapidly downstream of the grounding line with enhanced frictional drag. As in the idealized experiments, for $C_d = 16 \cdot {C_d}^0$ melt rates near the grounding line slightly exceed those along the outflow plumes. This is again indicative of the decorrelation of melt rates and thermal forcing in the velocity-dependent experiments. It can also be related to entrainment: as increased frictional drag increases the melt rates, enhanced mixed layer currents underneath the ice shelf result in more entrainment of water from below. As the temperature difference between the ice shelf base and ocean below and the shear related to the steepness of the ice shelf base are both highest near the grounding line, entrainment is expected to have the highest impact on melt rates there [*Little et al.*, 2009].

4. Discussion

Despite the higher level of complexity of the velocity-dependent melt rate parameterization compared to the velocity-independent version, the representation of physical processes involved in ice-ocean interactions, such as frictional drag due to rough surfaces or entrainment still deserves further attention. A number of aspects are discussed below.

4.1. Effects of roughness and frictional drag

The drag coefficient C_d in our model serves two purposes: (1) in a general sense, it captures a number of unresolved scales at the ice-ocean interface (and ocean bottom) that give rise to roughness and therefore exert a frictional drag on the flow, an effect represented via a stress term in the momentum equation; (2) in the thermodynamical melt rate parameterization it establishes a relationship between frictional forcing and melt rates.

Thermodynamic forcing: Varying C_d may be justified by the fact that its value is unknown and may depend on the material and morphological roughness properties of the interface considered. Increasing C_d by 4 times the default value to $C_d = 6 \cdot 10^{-3}$ in our model to approach published melt rate estimates is in line with *Jenkins et al.* [2010a], who increased C_d to $6.2 \cdot 10^{-3}$ to match their observational estimate of ablation rates underneath Ronne Ice Shelf. Although this number is at the high end of previously published values, melting near the grounding line in our velocity-dependent experiments remains low compared to recent estimates of melt rates under PIIS, locally in excess of 100 m/yr [*Payne et al.*, 2007; *Bindschadler et al.*, 2011; *Dutrieux et al.*, 2013]. Obtaining such high melt rates requires increasing C_d to 16 times its default value. Depending on the model, other parameters may be available for tuning observed melt rates. *Payne et al.* [2007] tuned their simulated melt rates by varying shelf core temperature, horizontal eddy viscosity, entrainment coefficient and drag parameter. Sensitivities of cavity-averaged melt rate were found to be largest with respect to drag and entrainment parameters (see their Figure 13).

Momentum forcing and vertical discretization: While the functional dependence of the melt rate on C_d simulated here (melt rates vary sub-linearly with drag coefficient) is in overall agreement with the plume model results of *Holland and Feltham* [2006] and *Payne et al.* [2007], an important difference is that we do not encounter a critical C_d value beyond which melt rates would decrease (which may be expected if excessive frictional drag impedes the plume flow). We attribute this to the different treatment of the frictional drag at the ice shelf base. In layer and plume models, the mixed layer (plume) depth and properties evolve in time and space. With increasing melt rates, larger volumes of buoyant meltwater are produced and the plume thickens and accelerates. However, with increasing drag, the impeding effect of friction on the plume dominates and the melting effectively decreases for very large values of drag.

In our z-level model, the drag does not act explicitly on the entire plume layer but only on the first grid cell below the ice-ocean interface. Further vertical mixing of momentum (i.e. the effect of the drag) and heat supply from below are parameterized by vertical diffusion (in our case even with constant coefficients) that may not be effective enough to form a thick plume. The acceleration by thermal forcing is mostly confined to the first grid cell layer and the counteracting drag is not strong enough for the flow to slow down. The sub-linear behavior of the mixed layer velocity in Figure 8c and Figure 8d shows that the negative feedback of increasing drag starts to act for high values of C_d. However, in the absence of a more sophisticated mixed-layer treatment, the negative feedback of drag onto the melt rates is not expected to be as important in level as in layer models.

Drag and geophysical roughness: Recent acoustic (Autosub) survey, laser altimetry, and radar data helped identify a network of basal channels with width on the order of 0.5 m to 3 km and height of up to 200 m on the underside of PIIS [*Bindschadler et al.*, 2011; *Vaughan et al.*, 2012; *Dutrieux et al.*, 2013; *Stanton et al.*, 2013]. These are thought to be formed near the grounding line, enlarged by basal melting downstream of the grounding line, and subsequently smoothed by melting towards the ice shelf front. *Dutrieux et al.* [2013] showed that the medium-scale (10 km) melt rates under PIIS are strongly modulated by melt variability at the scale of these channels. They reported high melting in channels near the grounding line, on the order of 40 m/yr (i.e., 80% more melting in channels than in keels) and lower channel melting of 15 m/yr in the region downstream. *Stanton et al.* [2013] also reported melting of approximately 20 m/yr at the apex of a basal channel under PIIS and near-zero melting on its flanks.

A number of studies related the formation and deepening of these features to an acceleration of mixed layer currents within the narrow channels leading to enhanced melting [*Vaughan et al.*, 2012; *Gladish et al.*, 2012; *Rignot and Steffen*, 2008; *Sergienko*, 2013].

These findings suggest that ice-ocean interactions are strongly modulated by kilometer-scale processes and imply that higher resolution models are required to accurately estimate both the spatial average and distribution of melting in ice shelf cavities.

One perhaps crude yet simple way of accounting for the effect of basal channels in large-scale models might be through the frictional drag. The studies mentioned above show that channel features, and hence the large-scale roughness characteristics of the base of PIIS are very heterogeneous. Associated with these channels are narrower surface and basal crevasses [*Vaughan et al.*, 2012], which further enhance the irregularity of the ice-ocean interface. While current velocity-dependent models employ a constant ice shelf basal drag coefficient, the use of a spatially varying value might be more appropriate to account for the distribution of these basal channels and crevasses.

4.2. Role of entrainment

Entrainment of warm waters by the buoyant plume as it rises along the ice shelf base can impact the melt rates in at least two ways. First, as the ambient ocean is warmer than the meltwater plume, entrainment raises the temperature of the plume and provides a heat source for melting. *Payne et al.* [2007] applied the reduced gravity plume model of *Holland and Feltham* [2006] to a realistic PIIS cavity and showed that buoyant plumes are indeed primarily fed by entrainment of warm waters near the grounding line. Second, *Holland and Feltham* [2006] identified that the inclusion of entrainment in their plume model decreases the relative importance of drag at the ice shelf base and therefore accelerates the plume. As the highest melt rates in our velocity-dependent model are collocated with the path of meltwater plumes, an increase in the speed of plume outflows would directly increase the maximum ablation rates.

The representation of entrainment in numerical models is very sensitive to the details of the vertical discretization. At scales typically considered (1 km and larger), the issue of too low entrainment is confined to layer (isopycnal or sigma) models (e.g., *Adcroft and Hallberg* [2006]), which therefore requires specific attention through adequate parameterizations. In contrast, *Legg et al.* [2006] and others have shown that level (z-coordinate) models typically suffer from excessive entrainment due to numerical diffusion, unless non-hydrostatic scales down to 1 to 10 m are resolved (e.g., *Sciascia et al.* [2013]). While tuning their plume model, *Payne et al.* [2007] found that entrainment had by far the largest effect on their predicted melt rates. In their model, melt rates increased monotonically with the entrainment coefficient such that any cavity-average target in the range of previously estimated melt rates for PIIS could be matched. In the present model, such tuning is not possible and entrainment by the meltwater plume cannot be easily quantified.

However, a shortcoming of plume models compared to three-dimensional baroclinic models is the need to prescribe ocean properties, hence not permitting an evolution of oceanic forcing, and not accounting for the effects of depth-independent flows within the cavity [*Holland and Feltham*, 2006]. *Payne et al.* [2007] justified their use of a plume model to simulate melt rates under PIIS by assuming that the control of barotropic flows on the redistribution of melting in “warm” ice shelf cavities might not be as important as in ”cold” and more weakly stratified cavities. The present experiments suggest, however, that the convergence of depth-independent currents along the steep cavity wall sets the location of the outflow plumes under PIIS.

4.3. Sensitivity to mixed-layer thickness

To test whether the spatial distribution and magnitude of melt rates obtained with our z-coordinate model depend strongly on the fixed thickness of the mixed layer, we conducted additional experiments in which we increased the vertical resolution of the model from 20 meters to 10 meters, and varied the thickness of the averaging layer for T_M, S_M and (U_M, V_M, W_M) between 10, 20 and 50 meters.

The melt rates simulated using ${C_d}^0$ are shown in Figure 10a–c for the velocity-independent and Figure 10d–f for the velocity-dependent experiments. Overall, the ablation pattern is maintained when varying the mixed layer depth. In the velocity-independent experiments, the maximum melt rates are located downstream of the grounding zone, while in the velocity-dependent simulations, melt rates are still highest along the path of the plume outflows, where currents underneath the shelf are strong.

As expected, the maximum melt rates increase with increasing thickness of the mixed layer. The velocity-dependent mean melt rate is nearly unchanged, while the velocity-independent mean melt rate increases slightly between the 10 and 20 meters cases. Larger changes in magnitudes only occur in the 50 meters velocity-independent case. This last case, however, is not used in the present study and is thought to overestimate the mixed layer thickness [*Jenkins et al.*, 2010a; *Stanton et al.*, 2013]. The decrease in mean and maximum melt rate with increasing vertical resolution was also observed by *Losch* [2008] (using a velocity-independent parameterization only). It is attributed to the fact that increasing the resolution decreases the total heat content of the grid cells adjacent to the ice shelf. Melting fills these cells with buoyant meltwater near the freezing temperature.

Therefore, higher vertical resolution at the ice shelf base (i.e., thinner cells) reduces the heat supply to the ice shelf from the ocean layer directly in contact with the ice shelf base.

In conclusion, our main result that the spatial distribution of the melting is very different between the velocity-dependent and velocity-independent melt rate parameterizations is not affected by the specified thickness of the mixed layer. Furthermore, mean melt rate magnitudes remain nearly unchanged (velocity-dependent) or change only slightly (velocity-independent) when changing from 10 m to 20 m mixed layer thickness. Therefore, our results appear to be affected only marginally by the inability of the model to account for the spatial and temporal variability of an evolving mixed layer near the ice shelf base.

5. Summary and conclusion

The goal of this study was to assess two parameterizations of turbulent heat and salt transfer at the base of an ice shelf in terms of the simulated sub-ice shelf cavity circulation and melt rate patterns in the context of a three-dimensional z-coordinate general circulation model. The first parameterization is based on the work of *Hellmer and Olbers* [1989]. It assigns constant values to the turbulent exchange velocities, $\gamma_{T,S}$, and hence implies constant ocean current speeds underneath the ice shelf. The second accounts for the turbulence generated by ocean currents at the ice interface and couples the turbulent exchange velocities with the mixed layer flow [*Holland and Jenkins*, 1999]. Our simulations exposed important differences between the velocity-dependent and velocity-independent parameterizations, particularly in terms of the distribution of melting. The main findings of our simulations are summarized as follows:

- Our velocity-dependent simulations differ significantly from previously-published ice shelf-ocean modeling studies using a velocity-independent melt rate parameterization. The experiments performed here suggest that, under conditions of current velocities and thermal forcing typical of PIIS or other "warm" ice shelves, the effects of parameterized turbulence in the proximity of the fixed ice interface dominate over those of temperature gradients in setting the diffusive heat flux through the ice-ocean boundary layer and, hence, the location of high melt rates. In our velocity-dependent experiments, the regions of largest melting coincide with strong outflow plumes and fast mixed layer currents, in agreement with *Payne et al.* [2007]. This is true over a range of two orders of magnitudes of drag coefficient values (1/16 to 8 times ${C_d}^0$), encompassing the values employed in published ice shelf-ocean interactions studies.

- Sensitivity experiments in which the drag coefficient is varied over this wide range of values indicate that the melt rate increases with $\sqrt{C_d}$ and reveal two important feedbacks on the melt rates. (1) They indicate a negative feedback due to the production of larger volumes of meltwater, which spreads at the shelf base and insulates the ice interface from the warmer water below. (2) They also indicate a positive feedback associated with the acceleration of geostrophic mixed layer currents, by increased buoyancy flux-induced density gradients underneath the ice shelf [*Little et al.*, 2008] and by stronger outflow plumes that feed on enhanced meltwater production. This second feedback is not accounted for in velocity-independent melt rate parameterizations. In the present velocity-dependent model, no critical value of C_d is found beyond which melt rates decrease with increasing drag coefficient because of the negative feedback of increased frictional drag on the mixed layer currents. Possible explanations for this behavior are strong buoyancy fluxes in our "warm" ice shelf simulations that dominate over friction in setting mixed layer velocities when increasing C_d, but also the treatment of friction in our z-coordinates, namely that friction is distributed over a fixed depth.

• No unique value of C_d reconciles the velocity-independent and dependent melt rates in both the idealized and realistic experiments. This suggests that feedbacks between melt rates, mixed layer velocities, and buoyancy fluxes depend on the details of the cavity geometry and restoring hydrographic properties. Similarly, optimal drag coefficients inferred from plume model simulations are not easily transferable to three-dimensional baroclinic models. For example, melt rates simulated using the velocity-dependent plume model of *Payne et al.* [2007] were in best agreement with an ice flux divergence calculation based on surface mass balance, ice thickness and ice flow data for $C_d = 3 \cdot 10^{-3}$. Their ice flux calculation indicated melt rates in excess of 100 m/y in a few localized regions, a PIIS proper average of 29.7 m/y, and a cavity average of about 20.7 m/y. Such melt rates require the use of $C_d \approx 6 \cdot 10^{-3}$ to $12 \cdot 10^{-3}$ in our realistic PIIS model.

A step toward ascertaining the relative contributions of ocean circulation, thermal forcing and entrainment in determining the location and strength of melting under PIIS may ultimately require non-hydrostatic simulations down to the scales of meters, and in the presence of tidal currents. The latter issue will be taken up elsewhere. Nevertheless, a robust result at present is the marked differences in melt rate patterns depending on whether velocity-dependent or independent transfer coefficients are used. Given the important implications on where within an ice shelf cavity the maximum melt rates are expected and their potential impact on ice shelf dynamical responses, our results call for more detailed observations that would resolve the spatial distribution of melt rates. First steps to this end have been made with the recent drilling through PIIS and deployment of a specialized suite of oceanographic instrumentation ("flux package"), measuring ocean velocity, temperature, and salinity at a sufficiently fast rate (4 Hz) so as to enable the inference of vertical turbulent fluxes of momentum, heat, and salt *Stanton et al.* [2013]. Such data hold the prospect of vastly improving constraints on turbulent transfer processes at the ice-ocean interface and improve melt rate parameterizations used in today's ocean climate models.

Appendix A: Thermodynamical melt rate parameterizations

Typical melt rate parameterizations are based on the assumption that phase changes at the ice-ocean boundary occur in thermodynamic equilibrium. The three-equation model uses two conservation equations for heat and salt, along with a third linearized relation [e.g., *Hellmer and Olbers*, 1989; *Holland and Jenkins*, 1999; *Jenkins et al.*, 2010a] that expresses the dependence of seawater freezing point temperature on salinity and pressure using empirical parameters a, b, c:

$$Q_I^T + Q_M^T = -L_f \rho_M \, m \tag{A1}$$

$$Q_I^S + Q_M^S = -\rho_M m S_B \tag{A2}$$

$$T_{\text{freeze}} = T_B(p_B, S_B) = a\, S_B + b\, p_B + c. \tag{A3}$$

Q_M^T and Q_M^S are the diffusive heat and salt fluxes across the ice-ocean boundary layer, Q_I^T and Q_I^S are the conductive heat flux and diffusive salt flux through the ice shelf, respectively, L_f is the latent heat of fusion/melting, ρ_M is the ocean mixed layer density, T_{freeze}, is the freezing temperature, T_B, S_B and p_B are the hydrographic properties and pressure at the ice shelf base, and m is the melt rate, expressed here as a volume flux per unit area (with corresponding mass flux $q = \rho_M\, m$).

In the present model, m is defined negative for melting and positive for refreezing (in contrast to *Holland and Jenkins* [1999]). All simulated melt rates reported here are expressed in terms of equivalent ice thickness. The salt in the ice shelf is neglected so that $Q_I^S = 0$ [*Eicken et al.*, 1994]. Following *Losch* [2008], we choose a salinity coefficient $a = -0.0575°\mathrm{C}$, a pressure coefficient $b = -7.61 \cdot 10^{-4}°\mathrm{C\ dBar}^{-1}$, and $c = 0.0901°\mathrm{C}$.

For a turbulent boundary layer, the turbulence-induced variability of the diffusivities of tracers $X = \{T, S\}$ may be represented by a non-dimensional Nusselt number, Nu:

$$Q_M^X = \rho_M c_{pM}^X \frac{\mathrm{Nu}\, \kappa_M^X}{D}(X_M - X_B), \tag{A4}$$

where c_{pM}^T is the heat capacity of the mixed layer (and $c_{pM}^S = 1$), κ_M^X are the thermal and salt diffusivities and D is the thickness of the boundary layer. The factors $\gamma_X = \frac{\mathrm{Nu}\kappa_M^X}{D}$ have dimensions of velocity and are referred to respectively as the turbulent heat and salt exchange or piston velocities (hereinafter, $\gamma_{T,S}$). We note that the description of the three-equation model in the Appendix of *Losch* [2008] contains errors. These have been corrected in the present formulation.

Together with these generic expressions for Q_M^T and Q_M^S in terms of $\gamma_{T,S}$, the set of equations (A1) – (A3) provides solutions for T_B, S_B and m. They are used to infer boundary conditions for the temperature (T) and salinity (S) tendency equations, represented here as a generic equation for tracer X:

$$\kappa \frac{\partial X}{\partial z}\bigg|_B = (\gamma_X - m)(X_B - X_M) \tag{A5}$$

with vertical diffusion κ [*Jenkins et al.*, 2001]. The heat and salt balances and associated sign conventions in our model are illustrated in Figure 1, the various variables and constants are listed in Table 1.

Appendix B: Accounting for drag at the ice-ocean interface

To account for the circulation-driven turbulent exchanges at the ice shelf base the piston velocities $\gamma_{T,S}$ are turned into functions of the frictional drag at the ice shelf base via a friction velocity, u_*, which is related to the velocity of ocean currents through a simple quadratic drag law of the form:

$$u_*{}^2 = C_d U_M^2, \tag{B1}$$

with C_d a dimensionless drag coefficient and $U_M = \sqrt{u_M^2 + v_M^2 + w_M^2}$, the magnitude of the mixed layer current velocity. The piston velocities are expressed as

$$\gamma_{T,S} = \Gamma_{T,S} u_* = \Gamma_{T,S} \sqrt{C_d}\, U_M, \tag{B2}$$

where Γ_T and Γ_S (hereinafter, $\Gamma_{T,S}$) are turbulent transfer coefficients for heat and salt, respectively. *Holland and Jenkins* [1999] formulated expressions for $\Gamma_{T,S}$ that include the effects of rotation and of melting and refreezing on the stability of the boundary layer:

$$\Gamma_{T,S} = \frac{1}{\Gamma_{Turb} + \Gamma_{Mole}^{T,S}}, \tag{B3}$$

with

$$\Gamma_{Turb} = \frac{1}{k} \ln\left(\frac{u_* \xi_N \eta_*^2}{f h_\nu}\right) + \frac{1}{2\xi_N \eta_*} - \frac{1}{k}, \tag{B4}$$

and

$$\Gamma_{Mole}^{T,S} = 12.5(\mathrm{Pr}, \mathrm{Sc})^{2/3} - 6. \tag{B5}$$

Here, Pr and Sc are the Prandtl and Schmidt numbers for seawater, k is the von Karman constant, f is the Coriolis parameter, ξ_N is a dimensionless stability constant, h_ν is the thickness of the viscous sublayer, estimated as $h_\nu = 5\frac{\nu}{u_*}$. η_* is the stability parameter, formulated in terms of a critical flux Richardson number and the Obukhov length. It is negative for a destabilizing and positive for a stabilizing buoyancy flux. Other parameter values adopted from *Holland and Jenkins* [1999] are listed in Table 1.

Two caveats regarding the velocity-dependent parameterization are worth mentioning. First, both *Jenkins* [1991] and *Holland and Jenkins* [1999] make the assumption of a hydraulically smooth interface. While this approach may be applicable over ablating portions of the ice shelf base, it might not be entirely adequate over regions of refreezing. Support for this assumption comes from the work of *McPhee* [1992] and *McPhee et al.* [1999], who measured turbulent transfers underneath sea ice over a wide variety of roughness characteristics. They found that turbulent transfers appear to be independent of the roughness of the ice-ocean interface. Uncertainties remain, nevertheless, regarding roughness characteristics of ice shelf-ocean interfaces. *Jenkins et al.* [2010a] pointed out that little observational evidence exists to date that supports the direct applicability of findings from sea ice studies to the ice shelf problem.

Second, using a quadratic drag law introduces an unknown drag coefficient C_d in eqn. (B2). Current observations do not provide enough information to allow estimating the drag and turbulent transfer coefficients independently [*Jenkins et al.*, 2010a].

Appendix C: Approximations to the velocity-dependent melt rate parameterization

Based on the sensitivity analyses performed by *Holland and Jenkins* [1999], some approximations were adopted in the implementation of velocity-dependent melt rate parameterization in the MITgcm. They are briefly summarized in the following.

• The heat flux through the ice shelf, Q_I^T is only described by vertical diffusion, i.e., vertical advection is neglected. In this case the gradient in ice temperature at the shelf base is linear and can be estimated as $\frac{\partial T_I}{\partial z}\big|_B = \frac{T_S - T_B}{h_I}$, with T_S the (constant) surface temperature of the ice shelf and h_I, the local thickness of the ice shelf. Sensitivity analysis of simulated melt rates to the parameterization of heat flux through the ice shelf by *Holland and Jenkins* [1999] suggest that for high melt rates, as those obtained in our "warm" idealized and realistic ice shelf experiments, omitting vertical advection increases the simulated melt rates by about 10% (see their Figure 7b and c). However, as this percentage varies very little over a wide range (2°C) of thermal driving (see their Figure 7c), we do not expect this choice to significantly impact our simulated melt patterns.

• As in *Holland and Jenkins* [1999], it is assumed that all phase changes occur at the ice-ocean boundary. The formation of sea ice in front of the ice shelf is not simulated. The formation of frazil ice through supercooling in the water column is not parametrized either. Neglecting this process is not expected to affect the cavity dynamics greatly, because regions over which the plume refreezes underneath both our "warm" idealized and realistic PIIS ice shelves are very limited.

• Following the argument of *Holland and Jenkins* [1999] that direct freezing onto the ice shelf base is limited, we neglect the effect of a destabilizing buoyancy flux on the freezing rate and set the stability parameter η_* in equation (B4) to 1 in the case of refreezing. Contrary to *Holland and Jenkins* [1999], we also neglect the stabilizing effect of melting on the boundary layer, and hence in the present model, $\eta_* = 1$ also in the case of melting. *Holland and Jenkins* [1999] compared melt rates computed both with and without taking into account the effects of stabilizing/destabilizing buoyancy fluxes. They found that the explicit calculation of η_* in eqn. (B4) changed the melt rates by less than 10% under "moderate" conditions of friction velocity and thermal driving (see eqn. (2)), which they identified as $u_* > 0.001$ m s^{-1} and $T_* < 0.5$°C.

The area-averaged friction velocity underneath both the idealized and realistic PIIS ice shelves is above 0.001 m s^{-1} for most values of C_d used in this study (Figures 8c and 8d). However, for all values of C_d employed here, the thermal driving is larger than 0.5°C (Figures 8e and 8f) and is representative of most "warm" ice shelves in contact with CDW [e.g., *Jacobs et al.*, 1996; *Payne et al.*, 2007; *Holland*, 2008; *Holland et al.*, 2008; *Jenkins et al.*, 2010a]. Hence, parameterizing the stabilizing or destabilizing effect of the melting or refreezing-induced buoyancy fluxes on the boundary layer underneath the ice shelf could impact our simulated melt rates. Furthermore, the relatively large melt rates and associated stabilizing buoyancy fluxes may significantly suppress mixing underneath the ice shelf and inhibit further melting.

Holland and Jenkins [1999] pointed out that solving for melt rates and $\gamma_{T,S}$ in the presence of a stability parameter requires a computationally expensive iteration. Whether the addition of this extra level of complexity is necessary to obtain accurate estimates of melt rates underneath "warm" ice shelves such as PIIS requires further studies.

Acknowledgments. This work was supported in part by NSF grant # 0934404 and NASA grant # NNX11AQ12G. V.D. gratefully acknowledges a Postgraduate Doctoral Scholarship from the National Sciences and Engineering Research Council of Canada and from the Fonds Québécois de la Recherche sur la Nature et les Technologies. We thank two anonymous reviewers for their detailed comments and suggestions.

References

Adcroft, A., and R. Hallberg (2006), On methods for solving the oceanic equations of motion in generalized vertical coordinates, *Ocean Modelling*, *11*(1-2), doi: 10.1016/j.ocemod.2004.11.006.

Adcroft, A., C. Hill, and J. Marshall (1997), The representation of topography by shaved cells in a height coordinate ocean model, *Monthly Weather Review*, *125*(9), 2293–2315.

Adcroft, A., C. Hill, J.-M. Campin, J. Marshall, and P. Heimbach (2004), Overview of the formulation and numerics of the MIT GCM, in *Proceedings of the ECMWF Seminar on "Recent developments in numerical methods for atmospheric and ocean modeling"*, pp. 139–150, Shinfield Park, Reading, UK.

Beckmann, A., H. H. Hellmer, and R. Timmermann (1999), A numerical model of the Weddell Sea: Large-scale circulation and water mass distribution, *Journal of Geophysical Research*, *104*(C10), 23,375–23,391.

Bindschadler, R., D. G. Vaughan, and P. Vornberger (2011), Variability of basal melt beneath the pine island glacier ice shelf, west antarctica, *Journal of Glaciology*, *57*(204), 581–595.

Determann, J. M., and R. Gerdes (1994), Melting and freezing beneath ice shelves: Implications from a three-dimensional ocean-circulation model, *Annals of Glaciology*, *20*, 413–419.

Dinniman, M. S., J. M. Klinck, and W. O. Smith Jr. (2007), Influence of sea ice cover and icebergs on circulation and water mass formation in a numerical circulation model of the Ross Sea, Antarctica, *Journal of Geophysical Research*, *112*(C11013), doi:10.1029/2006JC004036.

Dinniman, M. S., J. M. Klinck, and W. O. Smith Jr. (2011), A model study of Circumpolar Deep Water on the West Antarctic Peninsula and Ross Sea continental shelves, *Deep Sea Research, Part II*, *58*, 1508–1523, doi:10.1016/j.dsr2.2010.11.013.

Dutrieux, P., D. G. Vaughan, H. F. J. Corr, A. Jenkins, P. R. Holland, I. Joughin, and A. Fleming (2013), Pine Island Glacier ice shelf melt distributed at kilometers scales, *The Cryosphere*, *7*, 1543–1555, doi:10.5194/tc-7-1543-2013.

Eicken, H., H. Oerter, H. Miller, W. Graf, and J. Kipfstuhl (1994), Textural characteristics and impurity content of meteoric and marine ice in the Ronne Ice Shelf, Antarctica., *Journal of Glaciology*, *40*(135), 386–398.

Galton-Fenzi, B. K., J. R. Hunter, R. Coleman, S. J. Marsland, and R. C. Warner (2012), Modeling the basal melting and marine ice accretion of the Amery Ice Shelf, *Journal of Geophysical Research*, *117*(C09031), doi:10.1029/2012JC008214.

Gill, A. E. (1973), Circulation and bottom water production in the Weddell Sea, *Deep-Sea Research*, *20*, 111–140.

Gladish, C. V., D. M. Holland, P. R. Holland, and S. F. Price (2012), Ice-shelf basal channels in a coupled ice/ocean model, *Journal of Glaciology*, *58*(212), doi:10.3189/2012JoG12J003.

Grosfeld, K., R. Gerdes, and J. Determann (1997), Thermohaline circulation and interaction between ice shelf cavities and the adjacent open ocean, *Journal of Geophysical Research*, *102*(C7), 15,595–15,610, doi:10.1029/97JC00891.

Heimbach, P., and M. Losch (2012), Ajoint sensitivities of sub-ice-shelf melt rates to ocean circulation under the Pine Island Ice Shelf, West Antarctica, *Annals of Glaciology*, *53*(60), doi:10.3189/2012/AoG60A025.

Hellmer, H. H., and D. J. Olbers (1989), A two-dimensional model for the thermohaline circulation under an ice shelf, *Antarctic Science*, *1*(04), doi:10.1017/S095410208900490.

Holland, D. M., and A. Jenkins (1999), Modeling thermodynamic ice-ocean interactions at the base of an ice shelf, *Journal of Physical Oceanography*, *29*, 1787–1800.

Holland, D. M., and A. Jenkins (2001), Adaptation of an isopycnic coordinate ocean model for the study of circulation beneath ice shelves, *Monthly Weather Review*, *129*, 1905–1927.

Holland, D. M., S. S. Jacobs, and A. Jenkins (2003), Modelling the ocean circulation beneath the Ross Ice Shelf, *Antarctic Science*, *15*, 13–23, doi:10.1017/S0954102003001019.

Holland, P. R. (2008), A model of tidally dominated ocean processes near ice shelf grounding lines, *Journal of Geophysical Research*, *113*, doi:10.1029/2007JC004576.

Holland, P. R., and D. L. Feltham (2006), The effects of rotation and ice shelf topography on frazil-laden ice shelf water plumes, *Journal of Physical Oceanography*, *36*(12), 2312–2327.

Holland, P. R., A. Jenkins, and D. M. Holland (2008), The response of ice shelf basal melting to variations in ocean temperature, *Journal of Climate*, doi:10.1175/2007JCLI1909.1.

Holland, P. R., A. Jenkins, and D. M. Holland (2010), Ice and ocean processes in the Bellingshausen Sea, Antarctica, *Journal of Geophysical Research*, *115*(C05020), doi:10.1029/2008JC005219.

Jacobs, S. S., H. H. Hellmer, and A. Jenkins (1996), Antarctic ice sheet melting in the Southeast Pacific, *Geophysical Research Letters*, *23*(9), 957–960.

Jacobs, S. S., A. Jenkins, C. F. Giulivi, and P. Dutrieux (2011), Stronger ocean circulation and increased melting under Pine Island Glacier ice shelf, *Nature*, *4*, doi: DOI:10.1038/NGEO1188.

Jenkins, A. (1991), A one-dimensional model of ice shelf-ocean interaction, *Journal of Geophysical Research*, *96*, 20,671–20,677.

Jenkins, A., and D. M. Holland (2002), A model study of ocean circulation beneath Filchner-Ronne Ice Shelf, Antarctica: Implications for bottom water formation, *Journal of Geophysical Research*, *29*(8), doi:10.1029/2001GL014589.

Jenkins, A., H. H. Hellmer, and D. M. Holland (2001), The role of meltwater advection in the formulation of conservative boundary conditions at an ice-ocean interface, *Journal of Physical Oceanography*, *31*, 285–296.

Jenkins, A., K. W. Nicholls, and H. Corr (2010a), Observation and parameterization of ablation at the base of Ronne Ice Shelf, Antarctica, *Journal of Physical Oceanography*, *40*, doi:10.1175/2010JPO4317.1.

Jenkins, A., P. Dutrieux, S. S. Jacobs, S. D. McPhail, J. R. Perrett, A. T. Webb, and D. White (2010b), Observations beneath Pine Island Glacier in West Antarctica and implications for its retreat, *Nature Geoscience*, *3*, doi:10.1038/NGE0890.

Joughin, I., and R. B. Alley (2011), Stability of the West Antarctic ice sheet in a warming world, *Nature Geoscience*, *4*, 506–513, doi:10.1038/ngeo1194.

Joughin, I., B. E. Smith, and D. M. Holland (2010), Sensitivity of 21st century sea level to ocean-induced thinning of Pine Island Glacier, Antarctica, *Geophysical Research Letters*, *37*, doi:10.1029/2010GL044819.

Kusahara, K., and H. Hasumi (2013), Modeling Antarctic ice shelf responses to future climate changes and impacts on the ocean, *Journal of Geophysical Research*, doi: 10.1002/jgrc.20166.

Legg, S., R. Hallberg, and J. B. Girton (2006), Comparison of entrainment in overflows simulated by z-coordinate, isopycnal and non-hydrostatic models, *Ocean Modelling*, *11*(1-2), doi:10.1016/j.ocemod.2004.11.006.

Little, C. M., A. Gnanadesikan, and R. Hallberg (2008), Large-scale oceanographic constraints on the distribution of melting and freezing under ice shelves, *Journal of Physical Oceanography*, *38*, doi:10.1175/2008JPO3928.1.

Little, C. M., A. Gnanadesikan, and M. Oppenheimer (2009), How ice shelf morphology controls basal melting, *Journal of Geophysical Research*, *114*(C12007), doi: 10.1029/2008JC005197.

Losch, M. (2008), Modeling ice shelf cavities in a z coordinate ocean general circulation model, *Journal of Geophysical Research*, *113*(C08043), doi:10.1029/2007JC004368.

MacAyeal, D. R. (1984a), Numerical simulations of the Ross Sea tides, *Journal of Geophysical Research*, *89*(C1), 607–615.

MacAyeal, D. R. (1984b), Thermohaline circulation below the Ross Ice Shelf: A consequence of tidally induced vertical mixing and basal melting, *Journal of Geophysical Research*, *89*(C1), 597–606.

MacAyeal, D. R. (1985a), Tidal rectification below the Ross Ice Shelf, Antarctica, in *Oceanology of the Antarctic continental shelves*, *Antarctic Research Series*, vol. 43, edited by S. S. Jacobs, pp. 133–144, AGU.

MacAyeal, D. R. (1985b), Evolution of tidally triggered meltwater plumes below ice shelves, in *Oceanology of the Antarctic continental shelves*, *Antarctic Research Series*, vol. 43, edited by S. S. Jacobs, pp. 109–132, AGU.

Makinson, K., P. R. Holland, A. Jenkins, and K. W. Nicholls (2011), Influence of tides on melting and freezing beneath Filchner-Ronne Ice Shelf, Antarctica, *Geophysical Research Letters*, *38*, doi:10.1029/2010GL046462.

Makinson, K., M. A. King, K. W. Nicholls, and G. H. Gudmundsson (2012), Diurnal and semidiurnal tide-induced lateral movement of Ronne Ice Shelf, Antarctica, *Geophysical Research Letters*, *39*, doi:10.1029/2012GL051636.

Mankoff, K. D., S. S. Jacobs, S. M. Tulackzyk, and S. E. Stammerjohn (2012), The role of Pine Island Glacier ice shelf basal channels in deep-water upwelling, polynyas and ocean circulation in Pine Island Bay, Antarctica, *Annals of Glaciology*, *53*(60), doi:10.3189/2012AoG60A062.

Marshall, J., A. Adcroft, C. Hill, L. Perelman, and C. Heisey (1997a), A finite-volume, incompressible Navier-Stokes model for studies of the ocean on parallel computers, *Journal of Geophysical Research*, *102*(C3), 5753–5766, doi:10.1029/96JC02775.

Marshall, J., C. Hill, L. Perelman, and A. Adcroft (1997b), Hydrostatic, quasi-hydrostatic and nonhydrostatic ocean modeling, *Journal of Geophysical Research*, *102*(C3), 5733–5752, doi:10.1029/96JC02776.

McPhee, M. G. (1992), Turbulent heat flux in the upper ocean under sea ice, *Journal of Geophysical Research*, *97*, 5365–5379.

McPhee, M. G., G. A. Maykut, and J. H. Morison (1987), Dynamics and thermodynamics of the ice/upper ocean system in the marginal ice zone of the Greenland Sea, *Journal* *of Geophysical Research*, *92*(C7), 7017–7031, doi:10.1029/JC092iC07p07017.

McPhee, M. G., C. Kottmeier, and J. H. Morison (1999), Ocean heat flux in the central Weddell Sea during winter, *Journal of Physical Ooceanography*, *29*, 1166–1179.

McPhee, M. G., J. H. Morison, and F. Nilsen (2008), Revisiting heat and salt exchange at the ice-ocean interface: Ocean flux and modeling considerations, *Journal of Geophysical Research*, *113*(C06014), doi:10.1029/2007JC004383.

Mueller, R. D., L. Padman, M. S. Dinniman, S. Y. Erofeeva, H. A. Fricker, and M. A. King (2012), Impact of tide-topography interactions on basal melting of Larsen C Ice Shelf, Antarctica, *Journal of Geophysical Research*, *117*, doi:10.1019/2011JC007263.

Nicholls, E., K. W.and Abrahamsen, J. J. H. Buck, P. A. Dodd, C. Goldblatt, G. Griffiths, K. J. Heywood, N. E. Hughes, A. Kaletzky, G. F. Lane-Serff, S. D. McPhail, N. W. Millard, K. I. C. Oliver, J. Perrett, M. R. Price, C. J. Pudsey, K. Stansfield, M. J. Stott, P. Wadhams, A. T. Webb, and J. P. Wilkinson (2006), Measurements beneath an Antarctic ice shelf using an autonomous underwater vehicle, *Geophysical Research Letters*, *33*(L08612), doi:10.1029/2006GL025998.

Payne, A. J., P. R. Holland, A. P. Shepherd, I. C. Rutt, A. Jenkins, and I. Joughin (2007), Numerical modeling of ocean-ice interactions under Pine Island Bay's ice shelf, *Journal of Geophysical Research*, *112*, doi:10.1019/2006JC003733.

Pritchard, H. D., S. R. M. Ligtenberg, H. A. Fricker, D. G. Vaughan, M. R. van den Broeke, and L. Padman (2012), Antarctic ice-sheet loss driven by basal melting of ice shelves, *Nature*, *484*, 502–505, doi:doi:10.1038/nature10968.

Ramming, H. G., and Z. Kowalik (1980), Numerical modeling of marine hydrodynamics, in *Applications to dynamics physical processes, Oceanographic series*, vol. 26, Elsevier.

Rignot, E. (1998), Fast recession of a West Antarctic glacier, *Science*, *281*(5376), 549–551, doi:10.1126/science.281.5376.549.

Rignot, E., and S. S. Jacobs (2002), Rapid bottom melting widespread near Antarctic Ice Sheet grounding lines, *Science*, *296*, doi:10.1126/science.1070942.

Rignot, E., and K. Steffen (2008), Channelized bottom melting and stability of floating ice shelves, *Geophysical Research Letters*, *35*(L02503), doi:10.1129/2007GL031765.

Schodlok, M. P., D. Menemenlis, E. Rignot, and M. Studinger (2012), Sensitivity of the ice-shelf/ocean system to the sub-ice-shelf cavity shape measured by NASA Ice-Bridge in Pine Island Glacier, West Antarctica, *Annals of Glaciology*, *53*(60), doi:10.3189/2012AoG60A073.

Sciascia, R., F. Straneo, C. Cenedese, and P. Heimbach (2013), Seasonal variability of submarine melt rate and circulation in an east Greenland fjord, *Journal of Geophysical Research*, doi:10.1002/jgrc.20142.

Sergienko, O. V. (2013), Basal channels on ice shelves, *Journal of Geophysical Research Earth Surface*, *118*, 1342–1355, doi:10.1002/jgrf.20105.

Smedsrud, L. H., A. Jenkins, D. M. Holland, and O. A. Nost (2006), Modeling ocean processes below Fimbulisen, Antarctica, *Journal of Geophysical Research*, *11*(C01007), doi:10.1029/2005JC002915.

Stanton, T. P., W. J. Shaw, M. Truffer, H. F. J. Corr, L. E. Peters, K. L. Riverman, R. Bindschadler, D. M. Holland, and S. Anandakrishnan (2013), Channelized ice melting in the ocean boundary layer beneath Pine Island Glacier, Antarctica, *Science*, *341*(1236), doi:10.1126/science.1239373.

Timmermann, R., H. H. Hellmer, and A. Beckmann (2002a), Simulations of ice-ocean dynamics in the Weddell Sea 1. Model configuration and validation, *Journal of Geophysical Research*, *107*(C33025), doi:10.1029/2000JC000741.

Timmermann, R., H. H. Hellmer, and A. Beckmann (2002b), Simulations of ice-ocean dynamics in the Weddell Sea 2. Interannual variability 1985-1993, *Journal of Geophysical Research*, *107*(C33025), doi:10.1029/2000JC000742.

Timmermann, R., A. Le Brocq, T. Deen, E. Domack, P. Dutrieux, B. Galton-Fenzi, H. Hellmer, A. Humbert, D. Jansen, A. Jenkins, A. Lambrecht, K. Makinson, F. Niederjasper, F. Nitsche, O. A. Nost, L. H. Smedsrud, and W. H. Smith (2010), A consistent data set of Antarctic ice sheet topography, cavity geometry and global bathymetry, *Earth System Science Data*, *2*, doi:10.5194/essd-2-262-2010.

Timmermann, R., Q. Wang, and H. H. Hellmer (2012), Ice-shelf basal melting in a global finite-element sea-ice/ice-shelf/ocean model, *Annals of Glaciology*, *53*(60), doi:10.3189/2012AoG60A156.

Vaughan, D. G., H. F. J. Corr, R. A. Bindschadler, P. Dutrieux, H. Hilmar Gudmundsson, A. Jenkins, T. Newman, P. Vornberger, and D. J. Wingham (2012), Subglacial melt channels and fracture in the floating part of Pine Island Glacier, antarctica, *Journal of Geophysical Research*, *117*(F03012), doi:10.1029/2012JF002360.

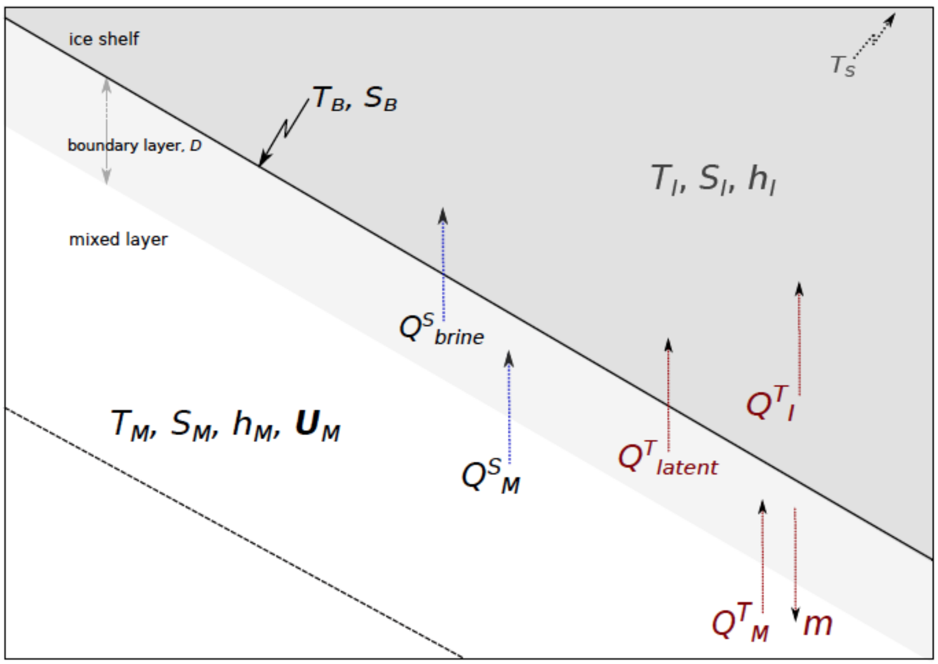

Figure 1. Schematic representation of the heat and salt balances at the base of an idealized ice shelf, as formulated in the present thee-equation model. The diagram represents an ice shelf of thickness h_I (dark grey shaded area), an ice-ocean boundary layer of thickness D at the ice shelf base and a mixed layer outside the boundary layer with fixed depth h_M. The sign convention is such that a positive (upward) heat flux through the boundary layer leads to melting (downward flux of freshwater) and a to positive conductive heat flux (upward) into the ice shelf. Q^T_M, Q^T_{latent} and Q^T_I have dimensions of a heat flux per unit volume (J ms^{-1} m^{-3} or Wm^{-2}). Q^S_M has dimensions of a flux of mass of salt per unit volume (kg ms^{-1} m^{-3}).

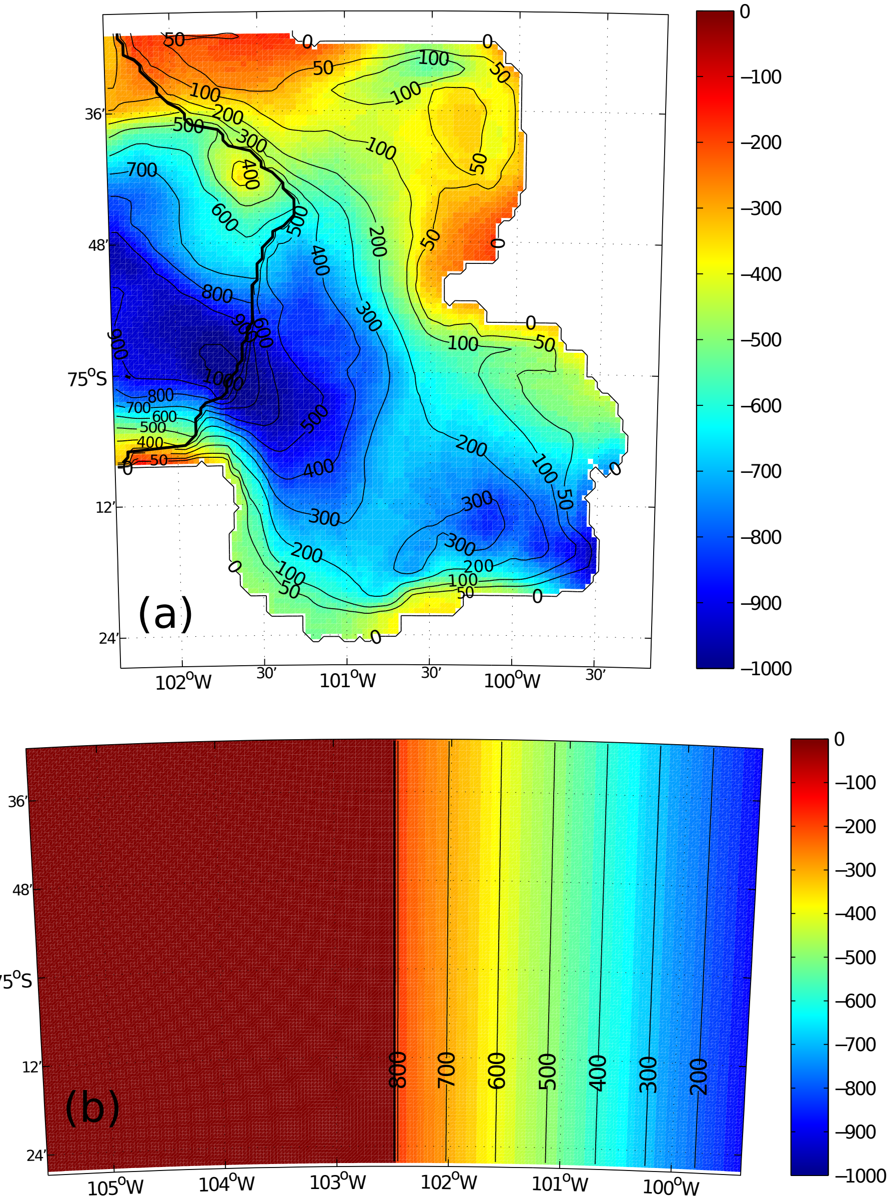

Figure 2. (a) Geometry of the ice shelf cavity in the realistic experiments. Shading is used for the bathymetry (m) and contours show the water column thickness (m). (b) Geometry of the idealized cavity. Shading indicates the depth of the ice shelf base (m) and contours, the water column thickness (m). The solid black line indicates the ice shelf front in both cases.

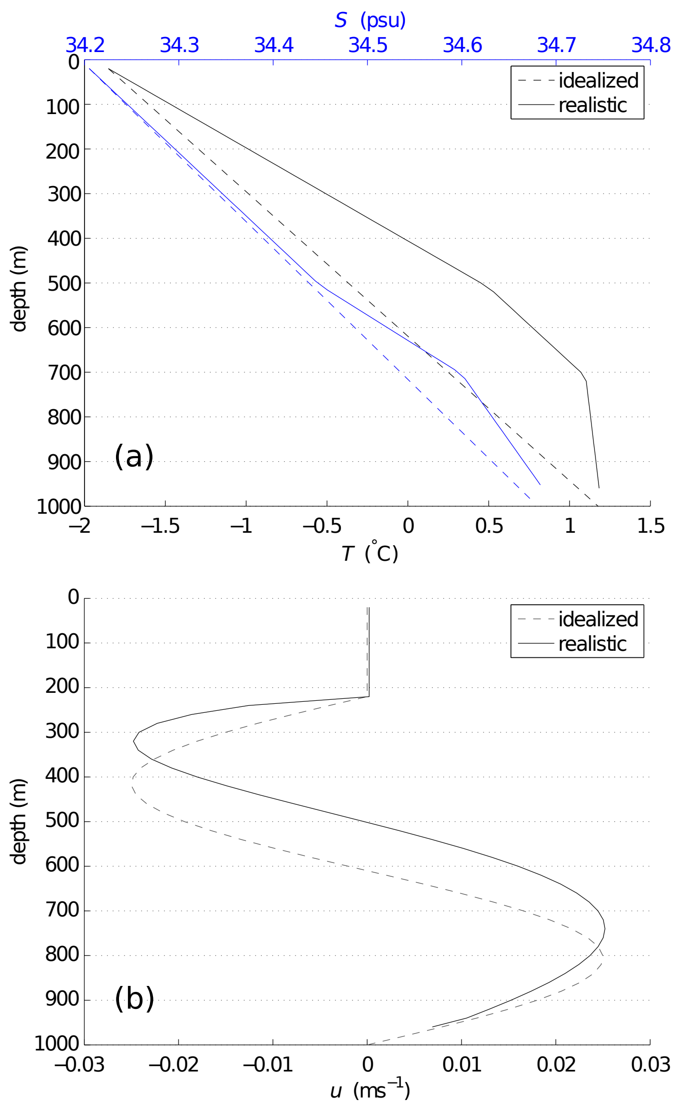

Figure 3. Vertical profiles of (a) temperature and salinity and (b) zonal velocity prescribed as the western open boundary conditions in the idealized and realistic experiments. Profiles are all uniform in the meridional direction.

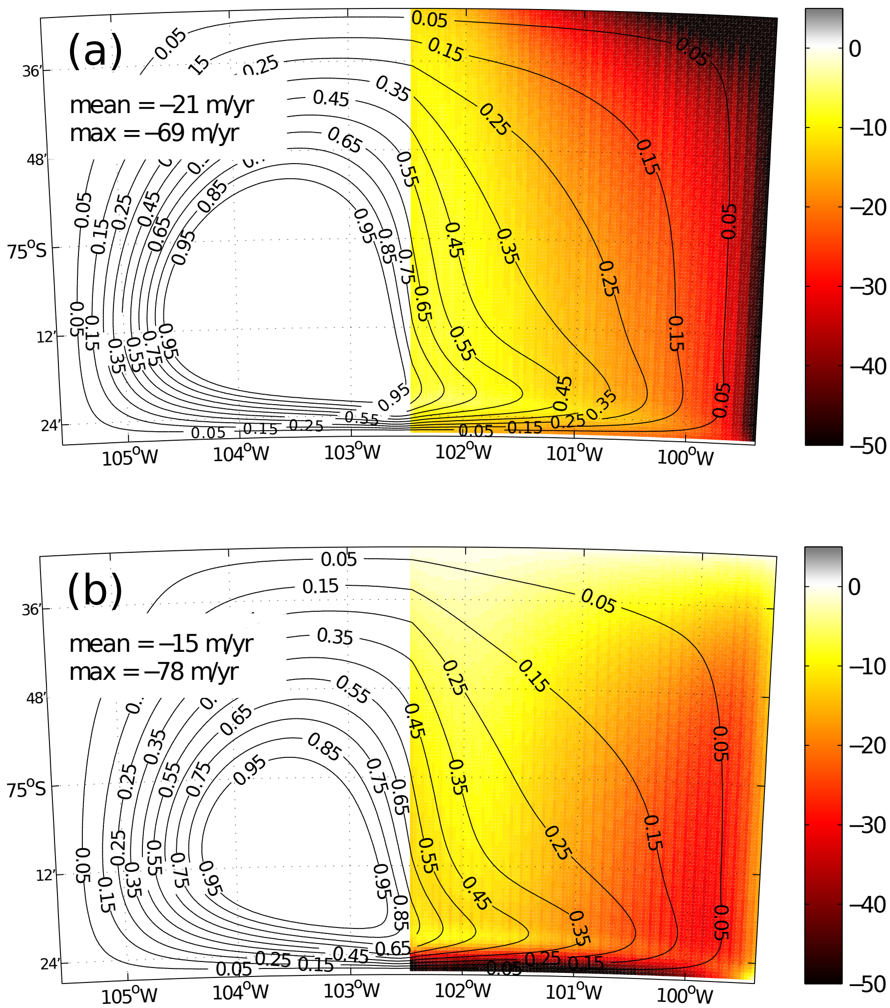

Figure 4. Melt rate (shading, in m/yr) and barotropic streamfunction for the depth-integrated horizontal volume transport (black countours, in Sv) in the idealized cavity setup using (a) the velocity-independent and (b) the velocity-dependent melt rate parameterization with ${C_d}^0$. The maximum and cavity-averaged melt rates are given in the top left corner of each panel.

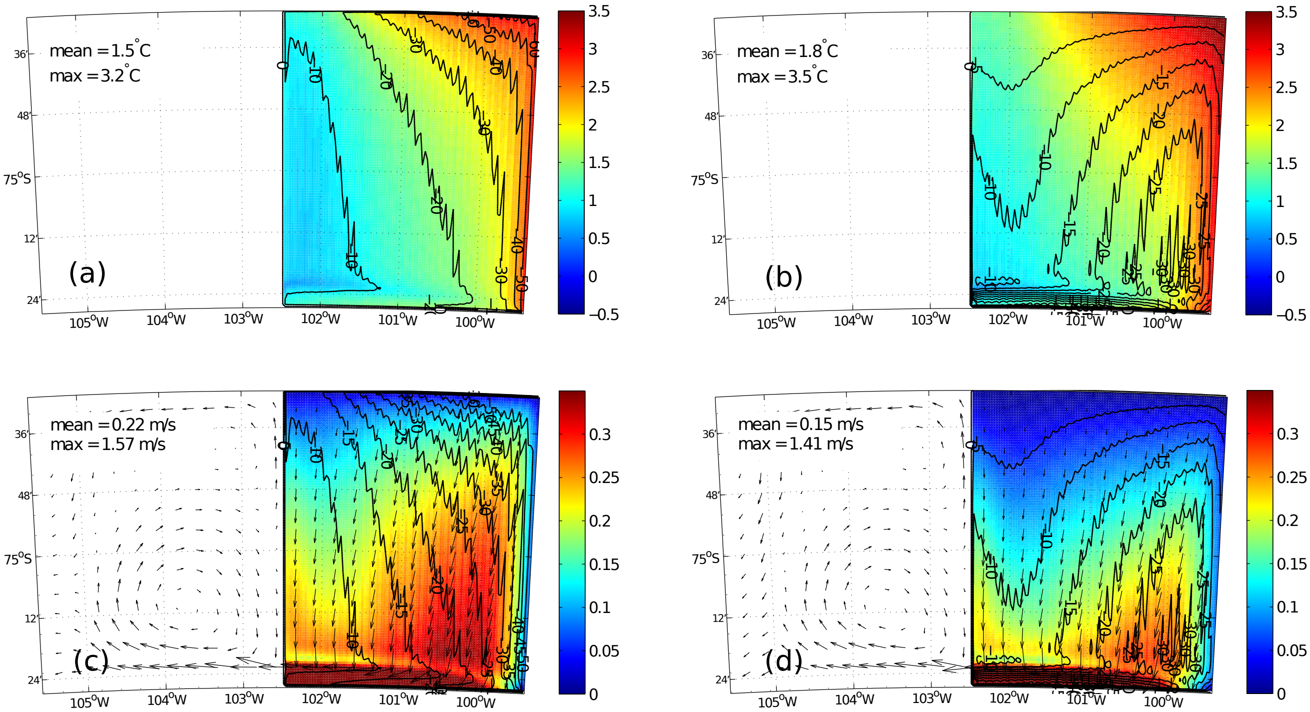

Figure 5. (a, b) Thermal forcing (C°) and (c, d) and ocean mixed layer velocity (m/s) in the idealized cavity setup with ${C_d}^0$. The values of area-averaged and maximum thermal forcing and mixed layer velocity are given in the top left corner of each figure. Black contours show the spatial distribution of melt rates (m/yr). Vectors indicate the direction and relative magnitude of the mixed layer currents on figures (c) and (d). Left panels show the the velocity-independent simulation results and right panels, results from the velocity-dependent simulation.

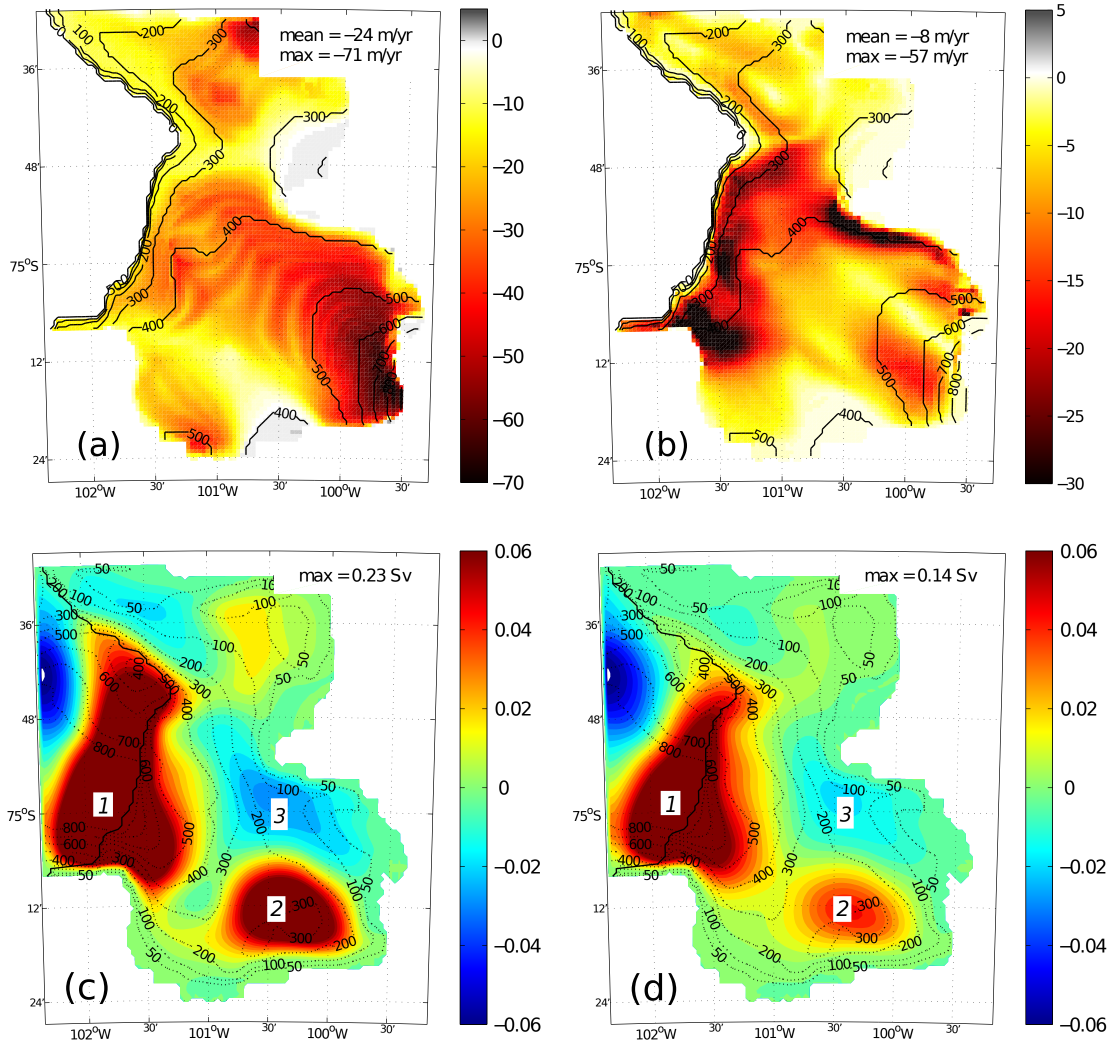

Figure 6. (a, b) Melt rate (m/yr) simulated using (a) the velocity-independent and (b) the velocity-dependent model in the realistic PIIS setup, with $C_d{}^0$. Black contours indicate the depth of the ice shelf base (m). The maximum and area-averaged melt rates are indicated in the top right corner of each panel. Different scales are used to bring out clearly the spatial distribution of melt rates in both cases. (c, d) Barotropic streamfunction for the depth-integrated horizontal volume transport (Sv) calculated using (c) the velocity-independent and (d) the velocity-dependent model. Dashed contours show the distribution of water column thickness (m) and the solid black line, the position of the ice shelf front. The three main depth-integrated ocean gyres discussed are indicated with numbers.

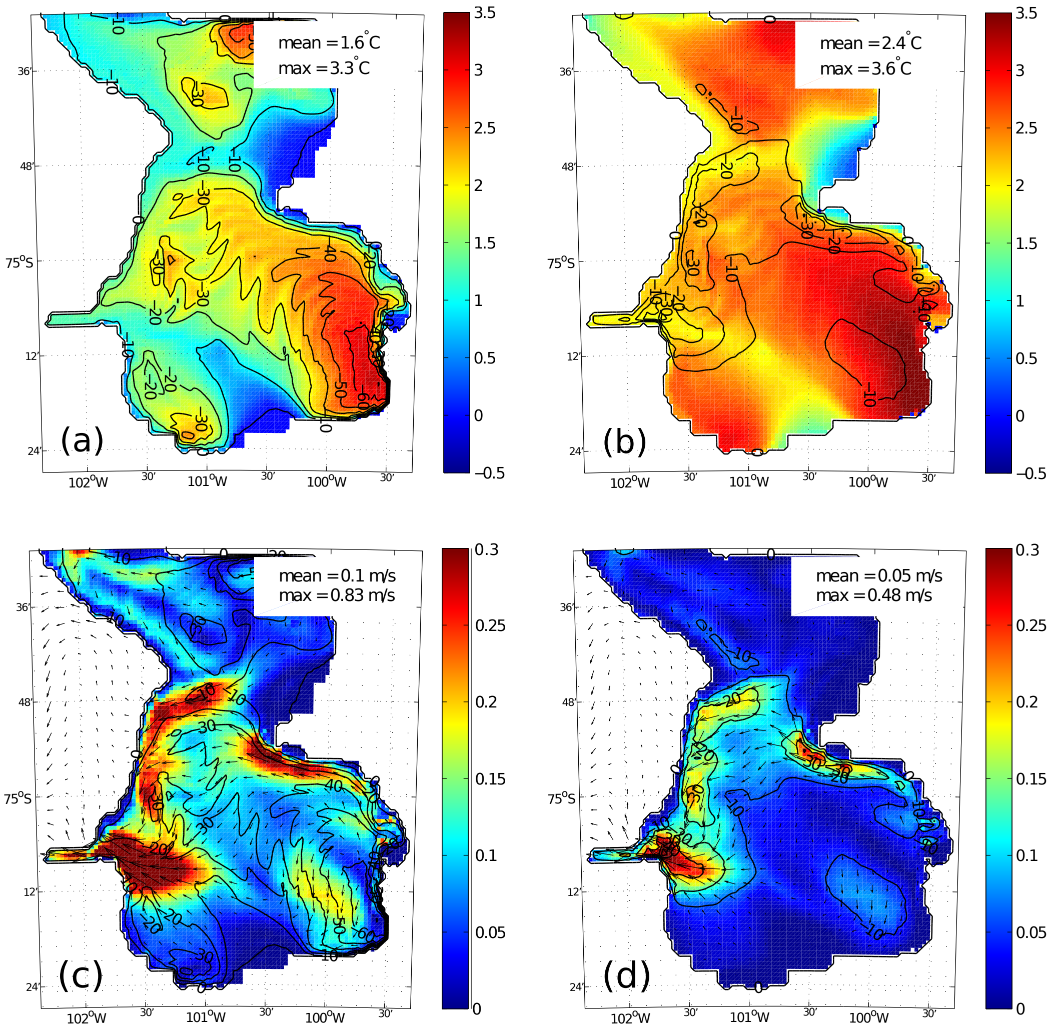

Figure 7. (a, b) Thermal forcing (C°) and (c, d) and ocean mixed layer velocity (m/s) in the realistic PIIS setup with ${C_d}^0$. Black contours show the spatial distribution of melt rates (m/yr) and the area-averaged and maximum values of the forcings are given at the top right corner of each panel. Vectors indicate the direction and relative magnitude of the mixed layer currents on panels (c) and (d). Left and right panels show the results from the velocity-independent and velocity-dependent simulation respectively.

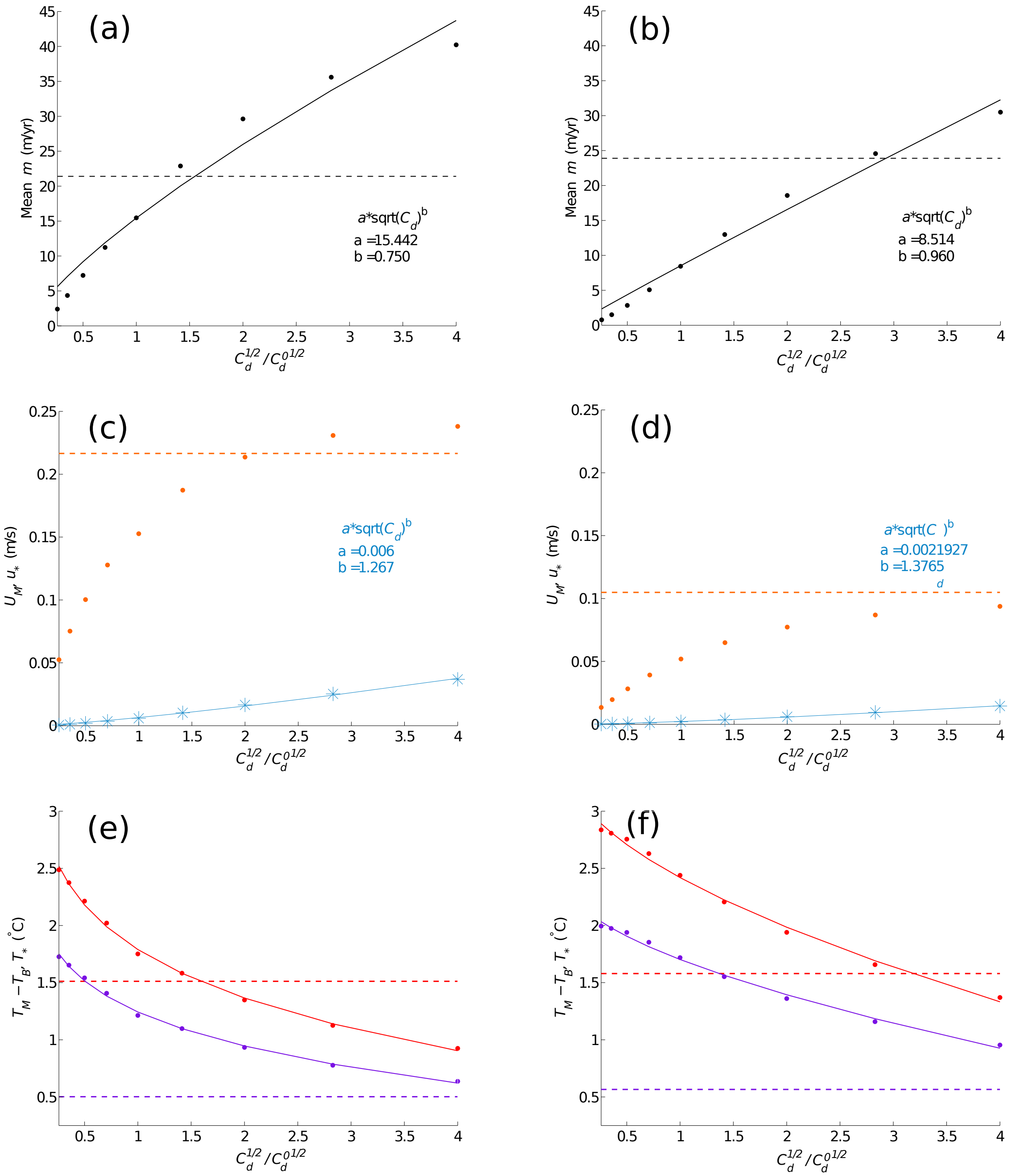

Figure 8. (a, b): Area averaged melt rate (m/yr, black dots) as a function of the square root of the drag coefficient $\sqrt{C_d}$ and power law fit (black curves, with coefficients in the lower right corner of the graph). The dashed black curve shows area averaged melt rates for the velocity-independent experiments with ${C_d}^0$. (c, d): Area averaged mixed layer velocity (m/s, orange dots) and friction velocity (m/s, blue asterisks), as a function of $\sqrt{C_d}$. The orange dotted line shows area-averaged mixed layer velocity U_M for the velocity-independent experiment with ${C_d}^0$. The solid blue curve is the power law fit to the area-averaged friction velocity. (e, f): Area averaged thermal driving (°C, red dots) and thermal forcing (°C, purple dots) across the boundary layer as a function of $\sqrt{C_d}$. The solid lines of the same colors are the corresponding power law fits. The red and purple dotted lines show respectively the area-averaged thermal driving and thermal forcing in the velocity-independent experiment with ${C_d}^0$. Left and right panels show the results of the idealized and realistic PIIS simulations, respectively.

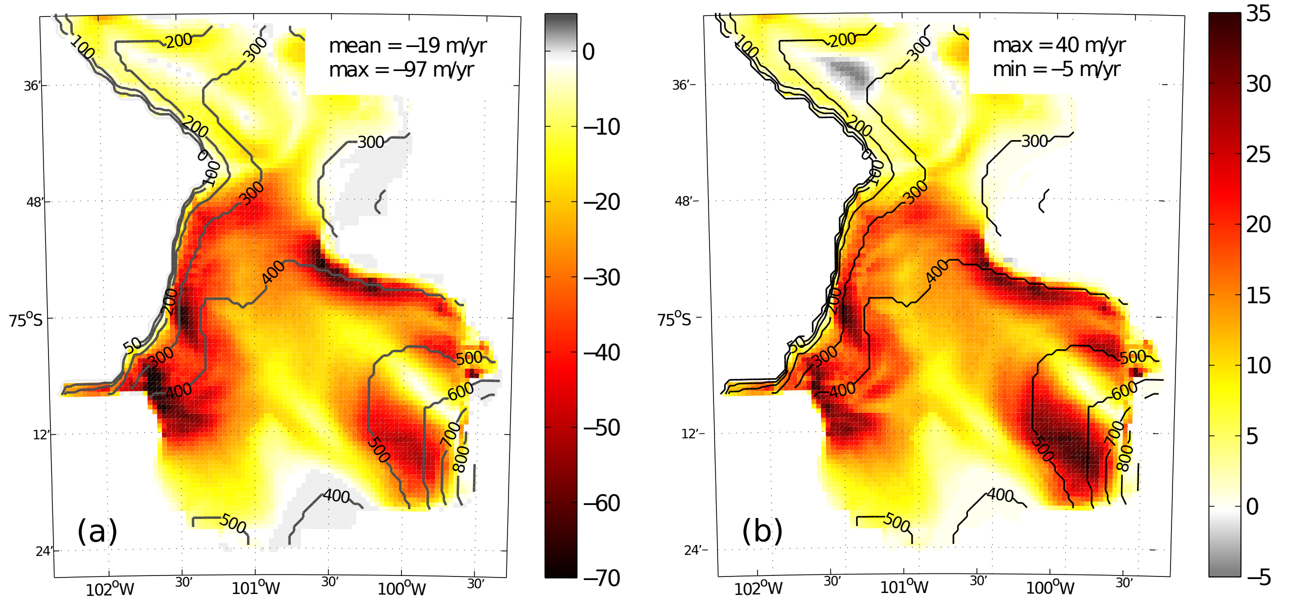

Figure 9. (a) Melt rate (m/yr) simulated using the velocity-dependent model in the realistic PIIS setup and $C_d = 4 \cdot {C_d}^0 = 6.0 \cdot 10^{-3}$. The maximum and area-averaged melt rates are indicated in the top right corner of the figure. For this value of drag coefficient, the area-averaged melt rate is comparable to the ice flux divergence based estimate of *Payne et al.* [2007] (20.7 m/yr). (b) Difference between the velocity-dependent melt rate simulated using $C_d = 4 \cdot {C_d}^0$ and ${C_d}^0$. Positive differences indicate a higher melt rate for the larger drag coefficient experiment. The maximum and minimum differences are indicated in the top right corner of the figure. Black contours indicate the depth of the ice shelf base (m) on both figures.

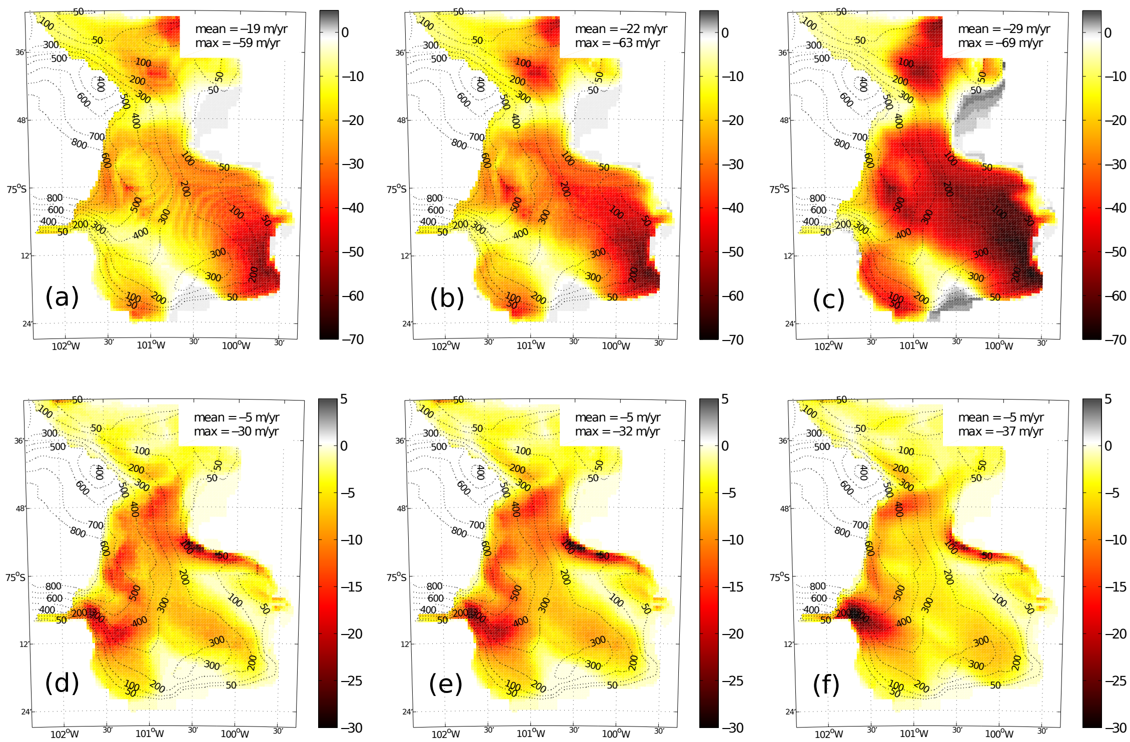

Figure 10. Melt rate (m/yr) simulated using (a to c) the velocity-independent and (d to f) the velocity-dependent model in the realistic PIIS setup with ${C_d}^0$ and a (a, d) 10 m, (b, e) 20 m and (c, f) 50 m thick mixed layer for averaging of T_M, S_M and U_M. Dashed contours show the distribution of water column thickness (m). The maximum and area-averaged melt rates are indicated in the top right corner of each panel.

Table 1. Three-equation model parameters and constants

Parameter	Symbol	Value
Ice shelf		
thickness	h_I	
surface temperature	T_S	$-20.0°$C
bulk salinity	S_I	0 psu
ice density		917 kg m^{-3}
heat capacity		2000 J kg^{-1} K^{-1}
molecular thermal conductivity		$1.54 \cdot 10^{-6}$ m^{2}s^{-1}
Ice-ocean boundary layer		
temperature	T_B	
salinity	S_B	
pressure	p_B	
Ocean mixed layer		
thickness	h_M	20 m (default)
temperature	T_M	
salinity	S_M	
water density	ρ_M	
specific heat capacity	$c_{p\,M}$	3998 J kg^{-1} K^{-1}
Latent heat of fusion	L_f	334000 J kg^{-1}
Latent heat flux	Q^T_{latent}	
Brine flux	Q^S_{brine}	
Diffuisve heat flux through the BL	Q^T_M	
Diffusive salt flux through the BL	Q^S_M	
Diffusive heat flux through the ice shelf	Q^T_I	
Diffusive salt flux through the ice shelf	Q^S_I	0
Melt/refreezing rate	m	
Transfer velocities parameterizations		
Turbulent transfer velocity for heat	γ_T	
Turbulent transfer velocity for salt	γ_S	
stability parameter	η_*	1.0
Von Karman's constant	κ	0.4
stability constant	ξ_N	0.052
kinematic viscosity of sea water	ν	$1.95 \cdot 10^{-6}$ m^{2}s^{-1}
Coriolis parameter	f	
Prandlt number	Pr	13.8
Schmidt number	Sc	2432
Model parameters		
Advection scheme		3^{rd} order direct space-time
Vertical advection and diffusion		Implicit for T and S
Equation of state		Jackett and McDougall (1995)
Vertical viscosity		10^{-3}m^{2}s^{-1}
Laplacian viscosity		0.2
Bi-harmonic viscosity		0.02
Vertical diffusion		$5 \cdot 10^{-5}$m^{2}s^{-1}
Horizontal diffusion		10 m^{2}s^{-1}
Quadratic bottom and shelf base drag	C_d	${C_d}^0 = 1.5 \cdot 10^{-3}$ (default)
Minimum partial cell factor		0.1 (1/8°), 0.3 (1/32°)
Reference ocean density,	ρ_{ref}	1000 kg m^{-3}

Table 2. Summary of experiments

Section	**setup**	$\gamma_{T,S}$ **formulation**	C_d
3.1.1	idealized	vel-dep. & indep.	${C_d}^0$
3.1.2	realistic	vel-dep. & indep.	${C_d}^0$
3.2.1	idealized	vel-dep.	$1/16$ to $16 \cdot {C_d}^0$
3.2.2	realistic	vel-dep.	$1/16$ to $16 \cdot {C_d}^0$